

4. Title and Subtitle Incorporation of Azimuthal Dependence in a Model of Strong Ground Motion		5. Report Date July 1985	
7. Author(s) C.C. Schoof; L.M. Shusto		8. Performing Organization Rept. No. FaAA-PA-R-85-07-17	
9. Performing Organization Name and Address Failure Analysis Associates 2225 East Bayshore Road P.O. Box 51470 Palo Alto, CA 94303		10. Project/Task/Work Unit No.	
		11. Contract(C) or Grant(G) No. (C) (G) CEE8460624	
12. Sponsoring Organization Name and Address Division of Industrial Science and Technological Innovation (ISTI) Directorate for Scientific, Technological, and International Affairs (STIA) National Science Foundation, Washington, DC 20550		13. Type of Report & Period Covered SBIR Phase I	
14.		15. Supplementary Notes	
16. Abstract (Limit: 200 words) <p>A necessary design element for buildings and other structures subjected to strong ground motions due to earthquakes is an estimate of the frequency and intensity of earthquakes expected to occur in the region during the economic life of the structure. It is also necessary to estimate the ground motion response at a site, given that an earthquake of a certain size and a certain distance away from the site occurs. Recognizing the random nature of earthquake occurrences, and the limited understanding of the physical processes leading to seismic loading at a site, analytical models have been developed to predict the probability of exceeding a given level of ground motion during a specified period. The report presents the results of initial (Phase I) efforts to refine and improve state-of-the-art models for predicting ground motion responses, and ultimately, to improve subsequent seismic hazard estimates.</p>			
17. Document Analysis a. Descriptors Earthquake resistant structures      Earthquakes Seismology      Design criteria Azimuth      Mathematical models			
b. Identifiers/Open-Ended Terms Ground motion Seismic hazard			
c. COSATI Field/Group			
18. Availability Statement NTIS		19. Security Class (This Report)	21. No. of Pages
		20. Security Class (This Page)	22. Price



INCORPORATION OF AZIMUTHAL DEPENDENCE IN A  
MODEL OF STRONG GROUND MOTION

Prepared by

Failure Analysis Associates  
Palo Alto, California

Dr. Craig C. Schoof  
Lisa M. Shusto

Prepared for

National Science Foundation  
Grant No. CEE-8460624

July 1985

Any opinions, findings, conclusions  
or recommendations expressed in this  
publication are those of the author(s)  
and do not necessarily reflect the views  
of the National Science Foundation.



## TABLE OF CONTENTS

<b>1.0</b>	<b>INTRODUCTION.....</b>	<b>1</b>
1.1	Strong Ground Motion Models.....	1
1.2	Azimuthal Variations in Strong Ground Motion Response.....	3
1.3	Theoretical Modeling of Strong Ground Motion.....	8
1.4	Phase I Objectives.....	10
<b>2.0</b>	<b>GROUND MOTION MODEL.....</b>	<b>12</b>
2.1	Analysis of Synthetic Acceleration Time Histories.....	14
2.2	Discussion.....	29
<b>3.0</b>	<b>AZIMUTHAL VARIATIONS IN OBSERVED STRONG GROUND MOTION RECORDS.....</b>	<b>30</b>
3.1	Ground Motion Modeling for the 1984 Morgan Hill Earthquake.....	30
3.2	Ground Motion Modeling for the 1980 Campania-Lucania Earthquake.....	35
3.3	Discussion.....	38
<b>4.0</b>	<b>STRONG GROUND MOTION ESTIMATION FOR SEISMIC HAZARD ANALYSIS.....</b>	<b>39</b>
4.1	Combination of Observed and Theoretical Information.....	39
4.2	Hazard Analysis for the Morgan Hill Region.....	44
4.3	Discussion.....	47
<b>5.0</b>	<b>RESULTS AND CONCLUSIONS.....</b>	<b>48</b>
	<b>REFERENCES.....</b>	<b>50</b>
	<b>APPENDIX A.....</b>	<b>56</b>
	<b>APPENDIX B - SIMULATED ACCELERATION TIME HISTORIES.....</b>	<b>59</b>
	<b>APPENDIX C - RECIPIENTS OF PHASE I RESEARCH RESULTS.....</b>	<b>61</b>

## ACKNOWLEDGMENTS

The authors wish to thank Ernest D. Eason and Jerrell M. Thomas for their critical review of the manuscript, and Professor Hareesh C. Shah for helpful discussions. The use of computer facilities at the John A. Blume Earthquake Engineering Center is gratefully acknowledged.

## 1.0 INTRODUCTION

A necessary design element for buildings and other structures subjected to strong ground motions due to earthquakes is an estimate of the frequency and intensity of earthquakes expected to occur in the region during the economic life of the structure. It is also necessary to estimate the ground motion response at a site, given that an earthquake of a certain size and a certain distance away from the site occurs. Recognizing the random nature of earthquake occurrences, and the limited understanding of the physical processes leading to seismic loading at a site, analytical models have been developed to predict the probability of exceeding a given level of ground motion during a specified period of time (Cornell, 1968; Esteva, 1969; McGuire, 1974; Der Kiureghian and Ang, 1975; Shah et al., 1975; Kiremidjian, 1976; Mortgat, 1976; and Campbell, 1977). These seismic hazard\* models have resulted in seismic design criteria that are consistent with the intended use (i.e., importance) and economic life of a given facility. Clearly, the success of such models in accurately predicting the seismic hazard at a site depends on the ability to accurately evaluate the ground motion response as a function of the size and location of a seismic event. This report presents the results of initial (Phase I) efforts to refine and improve state-of-the-art models for predicting ground motion responses, and ultimately, to improve subsequent seismic hazard estimates.

### 1.1 Strong Ground Motion Models

The characterization of strong ground motion response is shrouded in the complexities of fault rupture (non-uniform stress release along a fault; rupture initiation, propagation, stopping); the propagation of waves through an inhomogeneous, inelastic medium; and the local site characteristics (e.g., soil-structure interaction). In spite of these complexities, empirical models have been developed (e.g., Joyner and Boore, 1982; Campbell, 1981; Chiarottini and Siro, 1981; Herrmann and Geortz, 1981; Blume, 1977; McGuire, 1977 and

---

\* Seismic hazard is defined as the probability of exceeding a given level of ground motion during a given period of time.

Idriss, 1978) which provide ground motion scaling laws correlating the amplitude of the ground response with the size of the earthquake, and with the distance between the fault and the site.

The above scaling laws, sometimes referred to as attenuation laws or ground motion models, are developed by first defining the distance and size parameters (the independent variables) and response parameter (the dependent variable). The definitions for both dependent and independent variables are varied (see Boore and Joyner, 1982). This study focuses on one particular format for ground motion attenuation (Joyner and Boore 1981). This is given in equation 1.

$$Y = \log_{10}(\text{pga}) = c_1 + c_2 * M + c_3 * R - c_4 * \log_{10}(R) \quad (1)$$

where pga is the horizontal peak ground acceleration (the maximum value of two orthogonal accelerometer components),  $M$  is the moment magnitude, and  $R$  is defined as shown in equation 2:

$$R = (D^2 + k^2)^{1/2} \quad (2)$$

where  $R$  is the distance measured in km,  $D$  is the closest distance to the surface projection of the fault rupture in km, and  $k$  is an empirical constant, equal to 7.3 km.

The coefficients  $c_1$ - $c_4$  in equation 1 are evaluated using regression analysis.  $Y$  represents the mean value of  $\log_{10}(\text{pga})$ , and the residuals define the standard error of an assumed normal distribution in  $Y$  for given values of  $M$  and  $R$ .

The uncertainty in the predicted ground motion response, as defined by the standard error of the residuals, is assumed to account for factors in the ground motion model not accounted for in equation 1 as well as the underlying randomness of ground motion responses. These factors include:

- Variations in source characteristics for events of equal size

- Azimuthal variations in pga (e.g., radiation pattern, directivity)
- Variations in pga associated with the propagation path of seismic waves from the source to the site
- Variations in pga due to local site characteristics.

Because data from different seismogenic regions (e.g., varying earth structures, varying fault types) are often lumped together to perform the regression analyses, the variations in observed pga's associated with the factors above cannot be identified with a high level of confidence. Furthermore, other sources of bias (Table 1) prevent clear discrimination of the factors causing variations in pga. For these reasons, most ground motion models retain only the size and distance terms with an accompanying increase in the standard error. The impact of a large uncertainty in a ground motion estimate is clear; as the uncertainty in the ground motion estimate increases, the probability density associated with larger pga's increases. The net result is a greater predicted seismic hazard, resulting in higher seismic design loads. The ground motion at a site depends on the azimuth of the site with respect to the direction of rupture propagation.

In this study, the azimuthal dependence in horizontal peak ground accelerations is evaluated using simulated acceleration time histories from a theoretical source rupture/wave propagation model. Ultimately, provisions are made for incorporating azimuthal terms in strong motion prediction models, thereby minimizing systematic errors in predicted ground motion amplitudes. The following section describes two important mechanisms (radiation pattern and directivity focusing) which result in azimuthal-dependent ground motion response.

## **1.2 Azimuthal Variations in Strong Ground Motion Response**

The observed data that are used to develop empirical ground motion models represent an important source of information in estimating seismic hazards. At the same time there are other sources, namely seismological and geophysical theories concerning fault rupture processes and wave propagation, which should be utilized in the development of strong ground motion models. It is understood, for example, that the amplitude and phase of seismic waves

Table 1

---

Sources of Bias in Empirical Models

---

Various tectonic provinces

- differing earth structures
  - differing source mechanisms
  - differing anelastic attenuation properties
- 

Different instrumentation practices

- depth of embedment
  - soil-structure interaction effects
  - record processing
- 

Non-uniform distribution

- not enough events recorded close to the source
  - not enough large events
- 

emerging from a rupturing fault vary with the direction of wave propagation, depending on the geometry of the fault. In fact, this radiation pattern is used regularly to determine the earthquake focal mechanism. Conversely, if a predominant focal mechanism is known for a given source (i.e., its dip and slip angles), this information can be used to predict the variation in amplitudes of waves produced by that fault as a function of azimuth.

Figure 1 shows the radiation pattern for a vertical strike-slip fault. There are two four-lobed patterns in this figure; one for SH waves (horizontally-polarized shear waves) and one for P-SV waves (compressional and vertically-polarized shear waves). The amplitude of waves propagating at a given azimuth,  $\phi$ , is proportional to the radial distance from the origin to the appropriate curve. The SH waves have maximum amplitudes in the directions  $\phi = 0, \pi/2, \pi,$  and  $3\pi/2$ . At the same time, the P-SV waves theoretically have zero amplitude at these azimuths. However, if the ground motion model described in equation 1 is used to predict the wave amplitudes as a function of  $\phi$ , a circle would be plotted in Figure 1, as this model has no provision for azimuthal variations in amplitude.

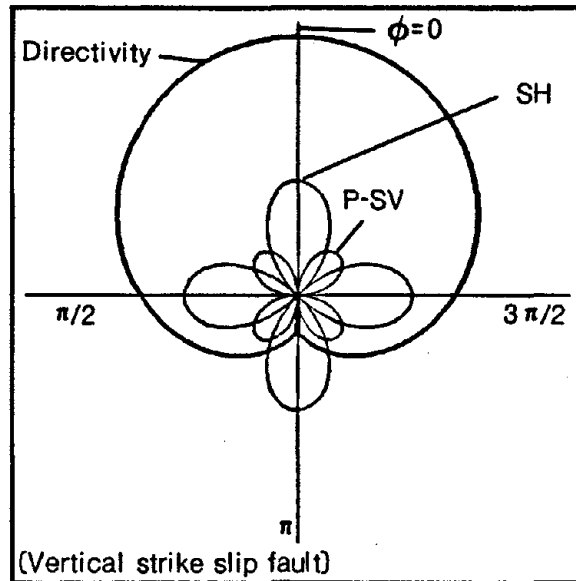


Figure 1. Azimuthal functions which scale the ground motion amplitudes: Radiation Patterns and Directivity Effects.

Directivity focusing is a second example where amplitudes and frequency content of waves leaving a source vary with azimuth. This phenomenon has been studied extensively (Singh, 1982, 1985; Boatwright and Boore, 1982; Bakun, et al., 1978; Boore and Joyner, 1978; and Schoof, 1984), and occurs when waves propagating from a distributed source with a moving rupture front (see Figure 2) interact, constructively at some frequencies and destructively at others. The result is that larger amplitude/higher frequency waves are generated in the direction of rupture propagation, and smaller amplitude/lower frequency waves propagate in the opposite direction. For a rupture propagating unilaterally from one end of a fault segment to the other, the wave amplitudes decrease monotonically between  $\phi = 0$  and  $\phi = \pi$ . Figure 3 (from Singh, 1981), shows how wave amplitudes vary with the rupture velocity (the Mach number,  $M$ , is equal to the rupture velocity,  $V_r$ , divided by the

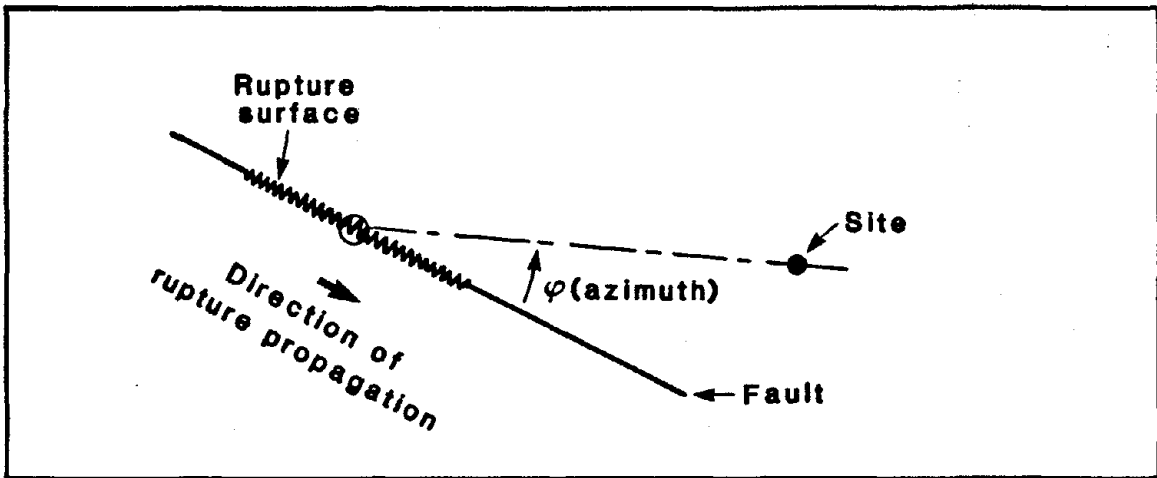


Figure 2. Schematic source/site configuration showing the site azimuth,  $\phi$ , measured with respect to the direction of rupture propagation.

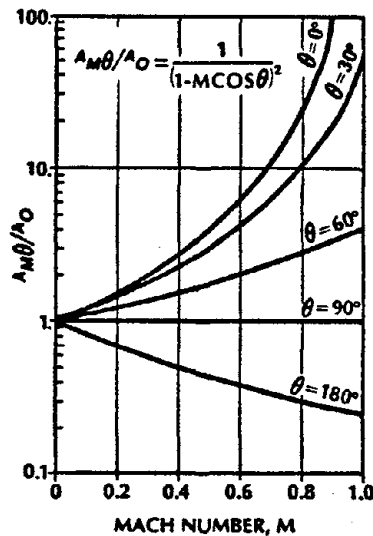


Figure 3. Amplitude scaling as a function of Mach number (rupture velocity divided by phase velocity) and as a function of azimuth,  $\theta$ , for a moving acoustical point source (from Singh, 1981). Amplitudes increase greatly in the direction of rupture propagation ( $\theta = 0$ ) as the Mach number approaches 1.

phase velocity,  $c$ , of the wave). As the rupture velocity approaches the phase velocity, the amplification due to directivity focusing increases dramatically, as does the ratio of amplitudes in the  $\phi = 0$  and  $\phi = \pi$  directions. The deamplification of amplitudes in the back-azimuth is less than the amplification at  $\phi = 0$  for all but very low rupture velocities. A directivity function as described would plot as a cardioid in the polar coordinate system shown in Figure 1. Figures 1 and 4, taken from Kasahara, 1981, show how the directivity function scales the radiation pattern of SH and P-SV waves from a strike-slip fault.

As noted previously, propagation path effects, local site effects, and generally sparse data make it difficult to resolve azimuthal effects in

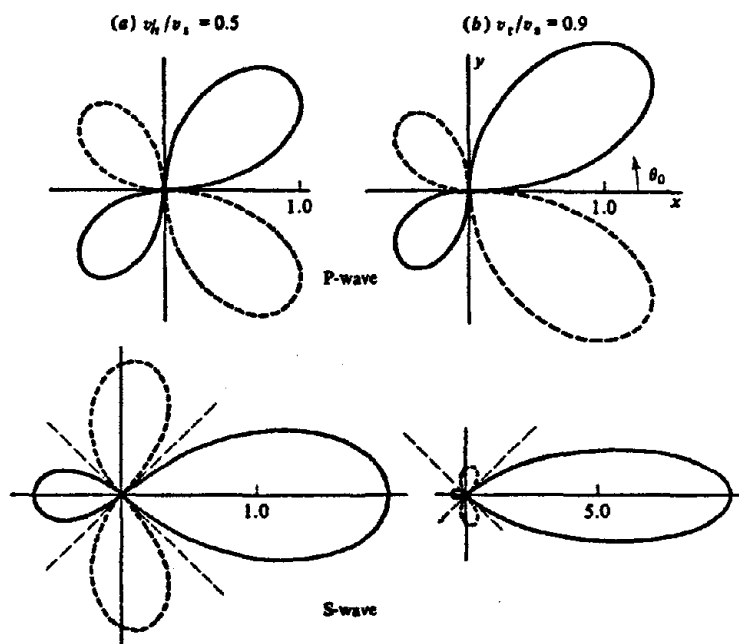


Figure 4. Effective radiation patterns for P and S waves for sources with a moving rupture front.

observed strong motion response. Therefore, a theoretical model for synthesizing large ensembles of strong motion records is used in this study to create an artificial data base for studying the effects of radiation pattern and directivity focusing.

### 1.3 Theoretical Modeling of Strong Ground Motion

A modal superposition technique is used to synthesize strong motion acceleration time histories. These time histories are generated taking into account the characteristics of the earth structure (such as the density and elastic moduli as a function of depth) as well as characteristics of the fault rupture process, rupture velocity, fault geometry and focal mechanism, seismic moment, and dislocation rise time. Both SH and P-SV waves are computed, corresponding to body waves as well as surface waves. Figure 5 outlines the procedure for simulating time histories using the normal mode method.

The normal mode method has been used to model long period time histories of displacement, velocity, and acceleration (Fukao and Abe, 1971; Herrmann and Nuttli, 1975; Swanger and Boore, 1978; and Wang and Herrmann, 1980), as well as high frequency (greater than 1 Hz) displacements and accelerations (McCann, 1981; Schoof, 1984). The ability of the modal superposition technique to represent observed ground motions has been demonstrated. An example comparing observed and simulated displacement and acceleration time histories from the 1968 Borrego Mountain earthquake is presented in Appendix A.

One of the difficulties in correlating azimuthal variations with observed ground motion responses in the empirical models in Section 1.2 is that the data (e.g., pga's) are typically too scarce and not distributed uniformly around the fault. This is not the case in numerical simulations, as time histories can be sampled at regular distance and azimuth intervals. In addition, irregular propagation path effects and local site effects are not present (nor are they possible) in the synthetics generated using this model. On one hand, this is an advantage, because it allows one to focus on

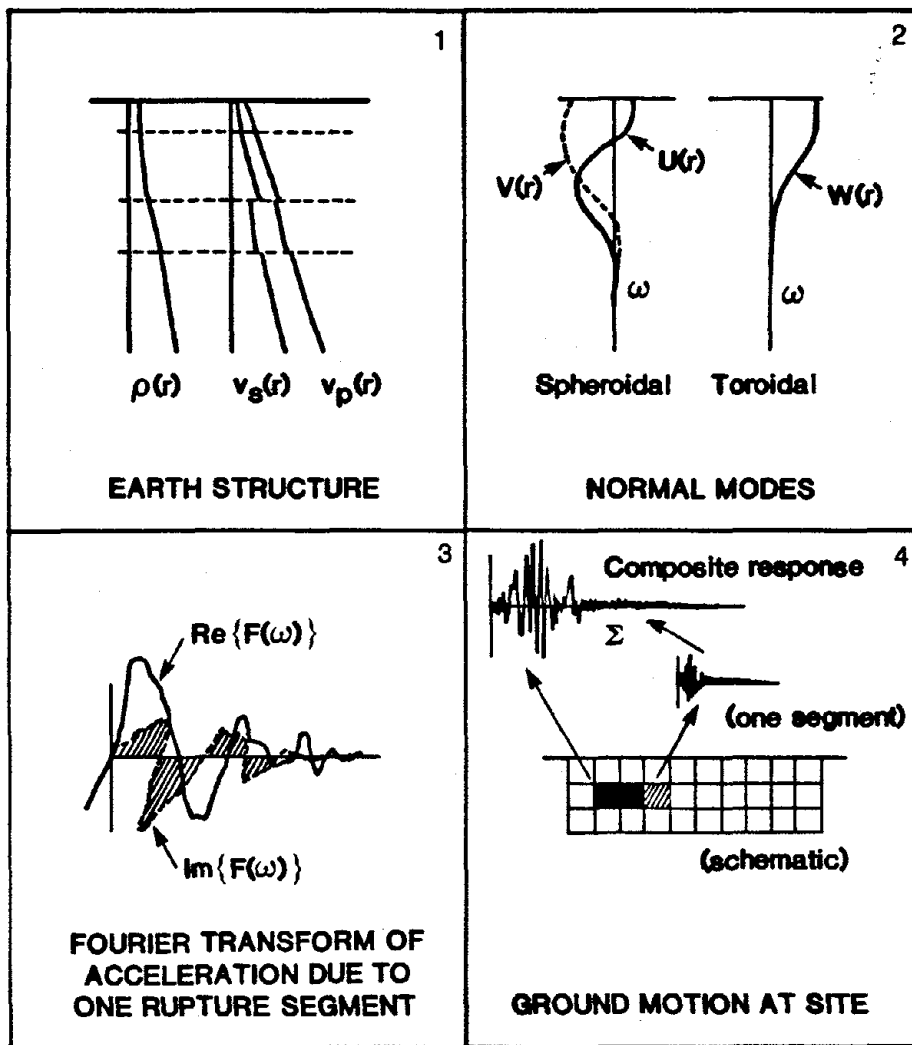


Figure 5. Procedure for computing normal mode synthetics.

1. Define earth structure for the region.
2. Normal modes are computed which depend on the earth structure only.
3. The Fourier transform of displacement or acceleration due to a point excitation is obtained as a linear combination of modal responses.
4. The site response is computed as a summation of responses from many point sources representing the fault rupture.

the azimuthal dependence in strong ground motion by separating out these other effects. At the same time, it is ultimately desirable to take into account all the factors contributing to the response at a particular site, including propagation path and site effects. For the case at hand, the normal mode method is well suited to address the issue of directionality in strong motion response.

Another compelling reason for utilizing the normal mode method is its relative efficiency in generating large numbers of time histories. The synthetic records are computed in two stages. First, the normal modes are evaluated for a given earth structure. This is a sizable task as approximately 5000-6000 modes must be computed. However, once completed, the same set of modes are used to simulate time histories by simply varying the source rupture parameters and site locations. The computation of the acceleration response for two horizontal components for a typical source made up of approximately 15 distinct rupture segments takes on the order of 30 seconds on an IBM 4381.

Other methods are available for simulating strong ground motion, including evaluation of the elastodynamic Green's function (Apsel, 1983) and various forms of ray tracing (e.g., Heaton and HelMBERGER, 1977). These methods become inefficient when complex earth structure is introduced (this is not the case in the normal modes approach), and neither method has a direct mechanism for accounting for anelastic attenuation. Furthermore, in these types of models, the entire computational process must be restarted for each simulation. These methods, as well as the normal mode method, become increasingly expensive as the upper frequency bound increases.

#### 1.4 Phase I Objectives

A primary goal of this work is to demonstrate that there exist viable sources of information which support a quantitative evaluation of the azimuthal dependencies in strong ground motion models. This study is intended to indicate justification for extending current ground motion models of the form  $\log_{10}(pga) = f_1(M) + f_2(R)$  to the form  $\log_{10}(pga) = f_1(M) + f_2(R) + f_3(\phi)$ .

The first task is to study the attenuation of pga as a function of R and  $\phi$  using a data base of synthetic acceleration records. The earth structure definition used to compute the normal modes corresponds to that of the Imperial Valley, although for the purposes of this investigation, any reasonable definition would have sufficed. Samples of the horizontal peak ground acceleration (the maximum of two orthogonal components) are obtained at regular distance intervals (every 5km between 10 and 80 km) and at regular azimuths (every  $\pi/10$  radians between 0 and  $\pi$  radians). For each event modeled,  $\phi$ -dependent and  $\phi$ -independent ground motion models are developed and compared.

Second, data from two earthquakes are studied in an attempt to identify azimuthal variations in horizontal peak ground accelerations. These earthquakes include the April 24, 1984, Morgan Hill earthquake in Northern California, and the November 23, 1980, Campania-Lucania earthquake in Southern Italy. The Morgan Hill earthquake was selected to test the concept of observable directivity focusing in strong motion acceleration records. The Italian earthquake, on the other hand, demonstrates a strong correlation with the radiation pattern associated with the normal faulting that occurred. As in Task I,  $\phi$ -dependent attenuation models are developed, which are then compared with  $\phi$ -independent ground motion models.

The final task is to provide guidelines for incorporating the results of Task I and Task II in the ground motion models to be used in a seismic hazard analysis. Clearly, the azimuthal dependencies in strong ground motion will vary from region to region, according to the types of faults (e.g., strike-slip vs. normal), the characteristics of the faults rupture process (e.g., unilateral vs. bilateral rupture propagation), and the particular earth structure.

The results of Tasks I, II, and III are presented in Sections 2, 3, and 4, respectively. A summary of the results and conclusions is presented in Section 5. Included in Section 5 is a discussion of the impact that azimuthal-dependent ground motion models will have on subsequent seismic hazard calculations.

## 2.0 GROUND MOTION MODEL

In order to account for azimuthal dependencies, the ground motion model in equation 1 is modified as shown in equation 3.

$$Y(M,R,\phi) = \log_{10}(pga) - f_1(M) + f_2(R) + f_3(\phi) \quad (3)$$

where M is the moment magnitude, R is as shown in equation 2, and

$$f_1(M) = a_1 * M \quad (4)$$

$$f_2(R) = b_1 * R + b_2 * \log_{10}(R) \quad (5)$$

$$f_3(\phi) = g_1(\phi) + g_2(\phi) \quad (6)$$

where  $g_1(\phi)$  includes terms corresponding to directivity focusing, and  $g_2(\phi)$  includes terms corresponding to the seismic radiation pattern. The function  $g_1(\phi)$  is assumed to be quadratic, which allows directivity scaling that is either monotonically decreasing from  $\phi = 0$  to  $\phi = \pi$  (as in a unilateral fault rupture) or as in the case of bilateral rupture, a scaling such that the amplitudes increase at  $\phi = 0$  or  $\phi = \pi$  while decreasing when  $0 < \phi < \pi$ . Function  $g_1(\phi)$  is shown in equation 7.

$$g_1(\phi) = d_1 + d_2 * \phi + d_3 * \phi^2 \quad (7)$$

The function  $g_2(\phi)$  depends on the type of fault rupture, and contains harmonic functions which account for the radiation pattern. For a vertical strike-slip fault,  $g_2(\phi)$  is

$$g_2^*(\phi) = r_1 + r_2 * |\sin 2\phi| + r_3 |\cos 2\phi| \quad (\text{vertical strike slip}) \quad (8)$$

For a normal fault,

$$g_2^{**}(\phi) = r_1 + r_2 * |\sin \phi| + r_2 |\cos \phi| \quad (\text{normal}) \quad (9)$$

While the functions  $g_2(\phi)$  are written as harmonics in the log scale, the shape of the normalized functions in the linear scale (for which they are originally defined) is adequate to represent variations associated with the seismic radiation pattern.

The site azimuth  $\phi$  is measured from the epicenter. This definition is used instead of the  $\phi$  corresponding to the closest rupturing segment because, when considering a site alongside a fault, the "closest-distance  $\phi$ " would always be  $\pi/2$ , even though the rupture may for the most part be propagating directly toward the site. However, it is most likely that there exists a point somewhere between the epicenter and the closest distance to rupture that would optimally define the effective distance and azimuth measures. For a vertical strike slip fault with a uniform distribution of energy release along the fault without directivity, it seems clear that the closest distance to fault rupture, and the  $\phi$  associated with this part of the fault, would be the appropriate spatial parameters. In this case, all sites between the fault endpoints have the same effective azimuth and the SH-wave radiation pattern amplitude (unity). However, when directivity plays an important role in the spatial distribution of amplitudes, the locations of points on the fault trace defining the effective distance and azimuth are uncertain. In fact, there may be one point defining the effective distance and a different point defining the effective azimuth. The analysis of the energy arriving at a site from each segment of a fault (e.g., using synthetic accelerograms) would help shed more light on this issue, and represents an important topic for future research.

Combining constants in equations 4, 5, 7 and 8 (considering only vertical strike-slip faults), and omitting the magnitude dependence, the ground motion model for the simulated events is

$$Y = c_1 + c_2 * R + c_3 * \log_{10}(R) + c_4 \phi + c_5 \phi^2 + c_6 |\sin 2\phi| + c_7 |\cos 2\phi| \quad (10)$$

The coefficients  $c_2$  and  $c_3$  are assumed to be known from previous ground motion studies, and are fixed in the regression model. From Joyner and Boore,  $c_2 = -0.00255$  and  $c_3 = -1.0$ . Therefore,

$$Y = c_1 -.00255*R - \log_{10}(R) + c_4\phi + c_5\phi^2 + c_6|\sin 2\phi| + c_7|\cos 2\phi|. \quad (11)$$

## 2.1 Analysis of Synthetic Acceleration Time Histories

A total of 990 acceleration time histories, representing 6 different earthquakes, were generated using the Imperial Valley earth structure as defined by Hamilton, 1970. Table 2 shows the density, shear wave velocity, and compressional wave velocity in each layer of the upper 20 km of the crust. The fault was assumed to be vertical strike-slip. Table 3 identifies the fault rupture characteristics for each event modeled. The moment magnitude for each simulation was 6.1, and the attenuation factor,  $Q^{\dagger}$ , was 200.

Table 2  
Imperial Valley Earth Structure

R(b)* (km)	$\rho$ (a) (g/cc)	$\rho$ (b) (g/cc)	$v_s$ (a) (km/s)	$v_s$ (b) (km/s)	$v_p$ (a) (km/s)	$v_p$ (b) (km/s)
6351.0	3.10	3.10	4.50	4.50	7.80	7.80
6359.5	3.00	3.00	4.10	4.10	7.10	7.10
6366.5	2.90	2.90	3.60	3.60	6.20	6.20
6368.15	2.50	2.50	2.50	2.50	4.30	4.30
6369.10	2.40	2.40	1.90	1.90	3.30	3.30
6370.45	2.20	2.20	1.40	1.40	2.40	2.40
6370.75	2.20	2.20	1.20	1.20	2.10	2.10
6371.00	2.00	2.00	1.00	1.00	1.70	1.70

\* R(b) is the radius at the top of the layer;  $\rho$ (a) corresponds to the density at the bottom of the layer. The variation  $\rho$ ,  $v_s$ , and  $v_p$  from the bottom to the top of a layer is assumed to be linear.

$\dagger$  analogous to structural damping

Table 3

## Fault Rupture Characteristics for Simulated Events

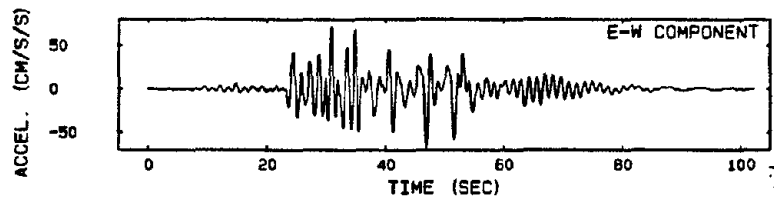
Simulation	Rupture Velocity (km/sec)	Rise Time (sec)	$L_0$ (km)	$L_\pi$ (km)	M
HHR0	1.9	0.50	10.0	4.0	6.1
HHR1	2.1	0.61	21.3	5.0	6.1
HHR2	2.1	0.66	38.6	4.1	6.1
HHR5	2.0	0.80	43.1	18.6	6.1
HHR6	1.5	0.80	43.1	2.6	6.1
HHR7	1.7	0.80	10.0	5.0	6.1

$L_0$  = Length of rupture in  $\phi = 0$  direction

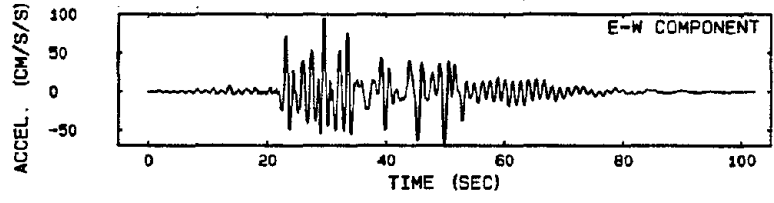
$L_\pi$  = Length of rupture in  $\phi = \pi$  direction

Figures 6 through 11 show sample time histories for event HHR6, where 6 through 8 are for sites in the  $\phi = 0$  direction (the direction of rupture propagation), and 9 through 11 are for sites in the  $\phi = \pi$  direction. Note that the amplitudes in the  $\phi = 0$  direction are much greater than those in the opposite direction. This is a result of the directivity focusing. These figures indicate an apparent contradiction in that the time histories toward  $\phi = 0$  do not show as much high frequency response as those in the back azimuth. What has happened in this event is the rupture velocity was such that the 1 Hz frequencies are greatly enhanced in the  $\phi = 0$  direction. Consequently, other higher frequencies do not show up appreciably when superimposed on the high-amplitude 1 Hz signal. The long period (~4 sec) Love waves noticeable at the end of the time histories for  $\phi = \pi$  are also present in the  $\phi = 0$  direction, and have approximately the same amplitude indicating that directivity has not appreciably affected the low frequency response.

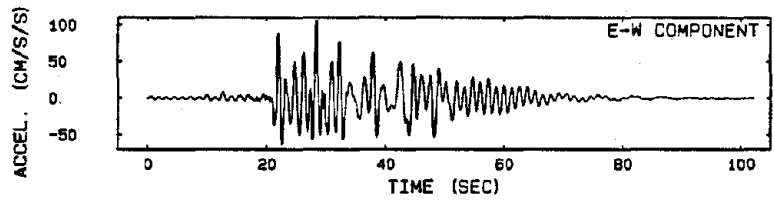
Another interesting point is that the peak amplitudes do not decrease monotonically with increasing source-to-site distance as all ground motion models suggest. For example, the peak amplitude at  $R = 55$  km and  $\phi = 0$  is 0.147g (Figure 7) while the peak at  $R = 50$  km  $\phi = 0$  is 0.121g. This reminds



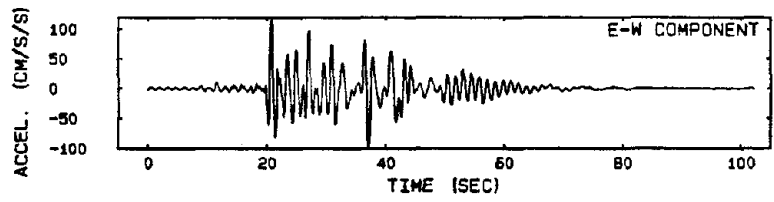
R: 80.0 PHI: 0.0 YM: 71.54  
 TAU: 0.7 VR: 1.9



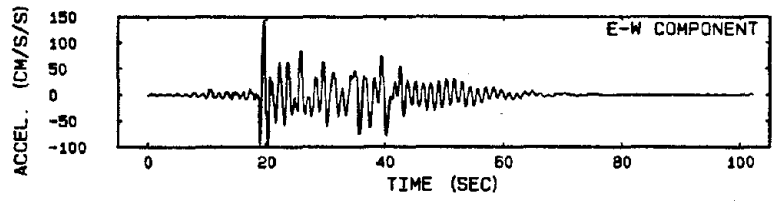
R: 75.0 PHI: 0.0 YM: 94.70  
 TAU: 0.7 VR: 1.9



R: 70.0 PHI: 0.0 YM: 105.71  
 TAU: 0.7 VR: 1.9

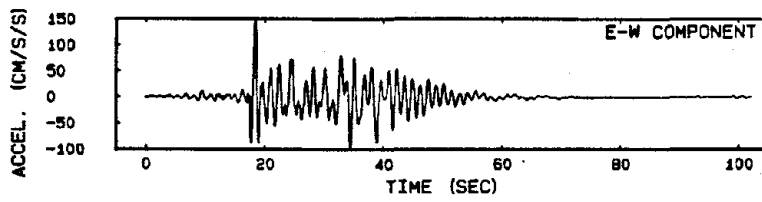


R: 65.0 PHI: 0.0 YM: 115.82  
 TAU: 0.7 VR: 1.9

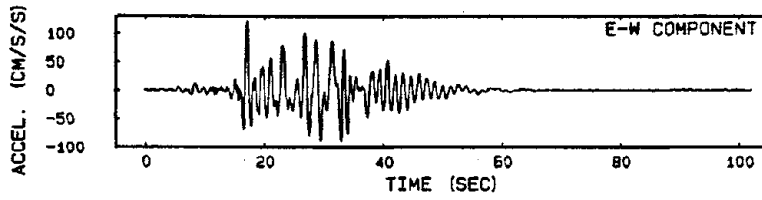


R: 60.0 PHI: 0.0 YM: 142.07  
 TAU: 0.7 VR: 1.9

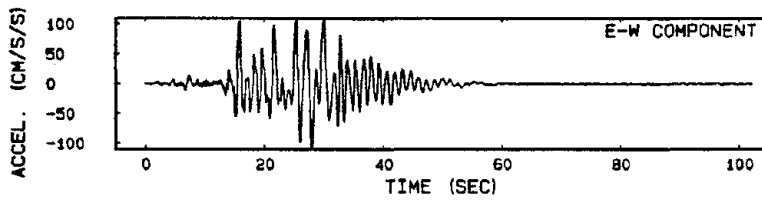
Figure 6. Simulated acceleration time histories for source HHR6 at sites along the direction of rupture propagation. Epicentral distances are 80, 75, 70, 65 and 60 km from top to bottom.



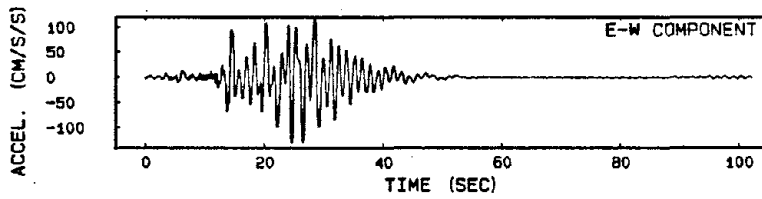
R: 55.0 PHI: 0.0 YM: 147.06  
 TAU: 0.7 VR: 1.9



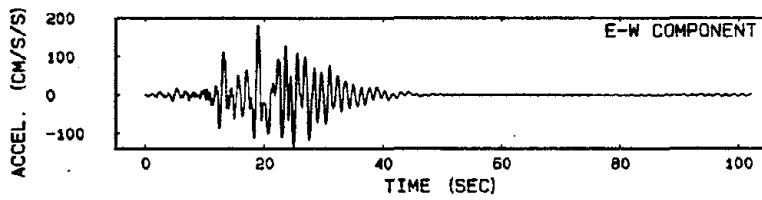
R: 50.0 PHI: 0.0 YM: 121.49  
 TAU: 0.7 VR: 1.9



R: 45.0 PHI: 0.0 YM: 109.67  
 TAU: 0.7 VR: 1.9

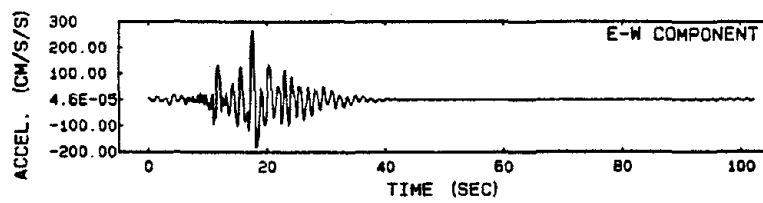


R: 40.0 PHI: 0.0 YM: 131.86  
 TAU: 0.7 VR: 1.9

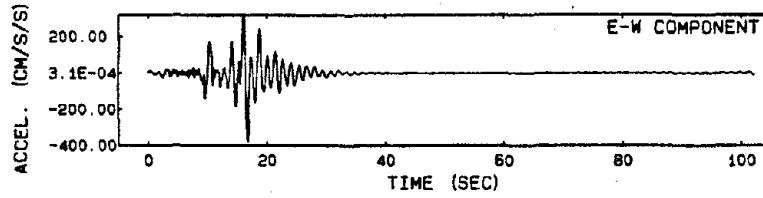


R: 35.0 PHI: 0.0 YM: 180.32  
 TAU: 0.7 VR: 1.9

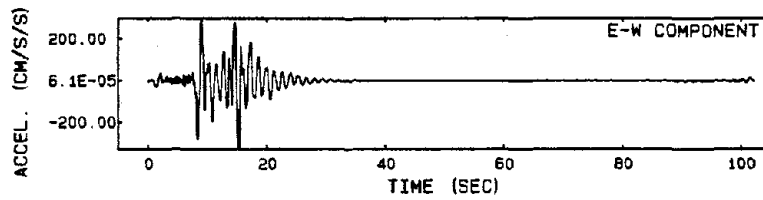
Figure 7. Simulated acceleration time histories for source HHR6 at sites along the direction of rupture propagation. Epicentral distances are 55, 50, 45, 40, and 35 km from top to bottom.



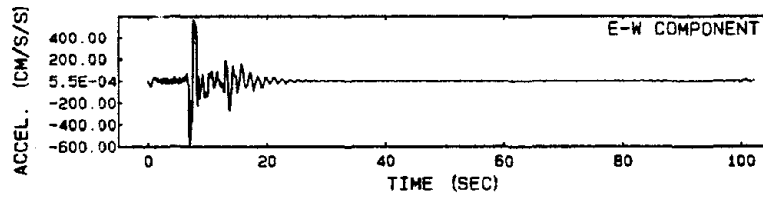
R: 30.0 PHI: 0.0 YM: 266.97  
 TAU: 0.7 VR: 1.9



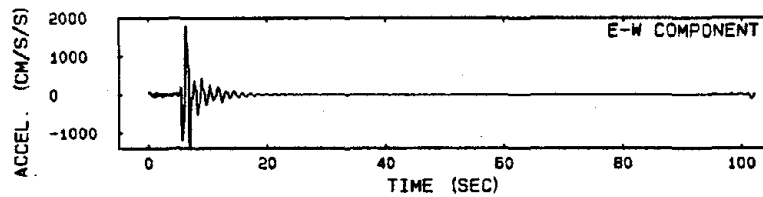
R: 25.0 PHI: 0.0 YM: 378.76  
 TAU: 0.7 VR: 1.9



R: 20.0 PHI: 0.0 YM: 322.90  
 TAU: 0.7 VR: 1.9

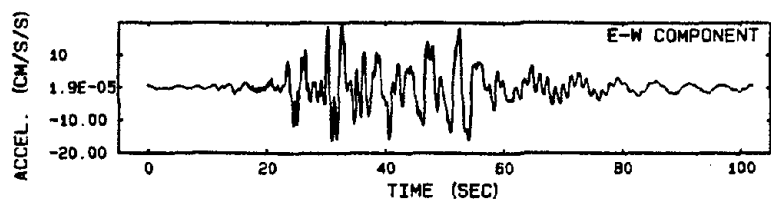


R: 15.0 PHI: 0.0 YM: 588.95  
 TAU: 0.7 VR: 1.9

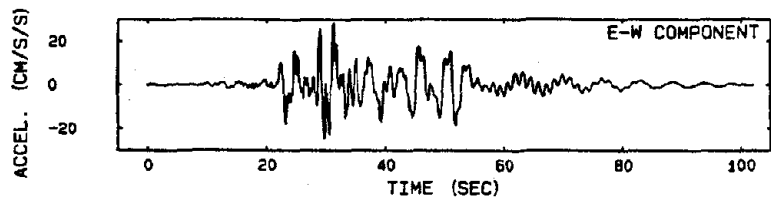


R: 10.0 PHI: 0.0 YM: 1815.71  
 TAU: 0.7 VR: 1.9

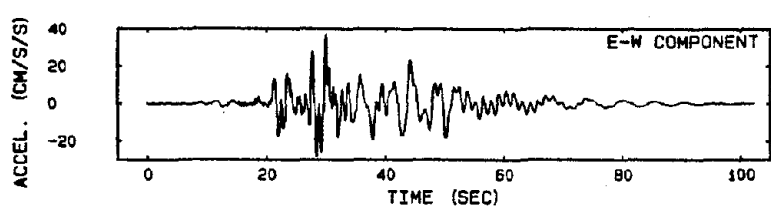
Figure 8. Simulated acceleration time histories for source HHR6 at sites along the direction of rupture propagation. Epicentral distances are 30, 25, 20, 15, and 10 km from top to bottom.



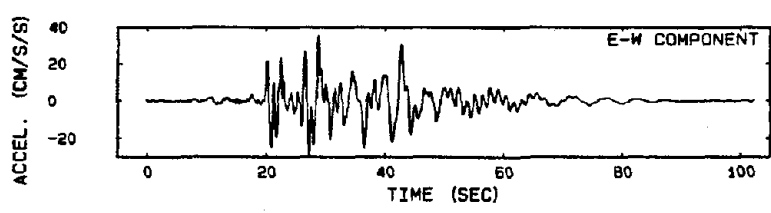
R: 80.0 PHI: 3.1 YM: 19.62  
 TAU: 0.7 VR: 1.9



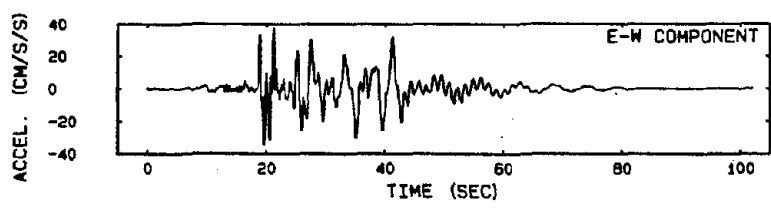
R: 75.0 PHI: 3.1 YM: 28.63  
 TAU: 0.7 VR: 1.9



R: 70.0 PHI: 3.1 YM: 37.21  
 TAU: 0.7 VR: 1.9

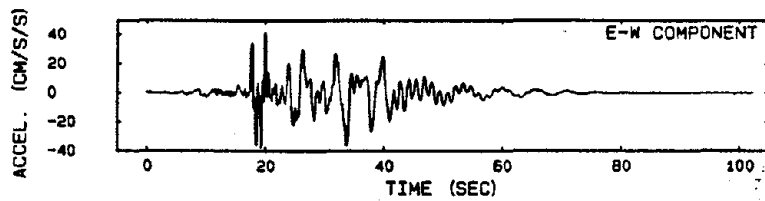


R: 65.0 PHI: 3.1 YM: 35.33  
 TAU: 0.7 VR: 1.9

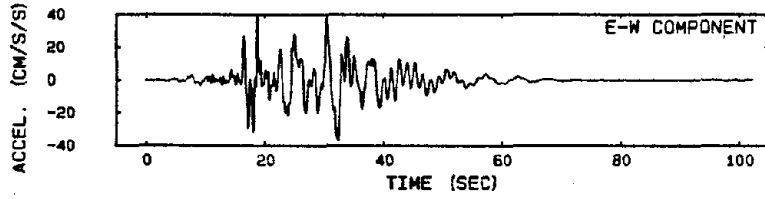


R: 60.0 PHI: 3.1 YM: 37.53  
 TAU: 0.7 VR: 1.9

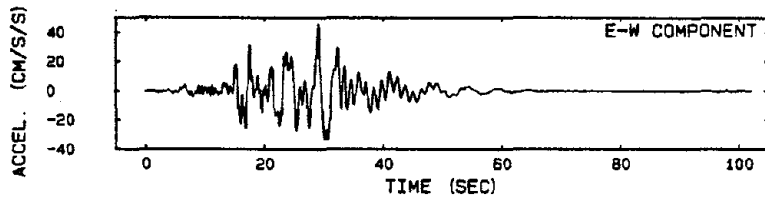
Figure 9. Simulated acceleration time histories for source HHR6 at sites along the direction away from rupture propagation. Epicentral distances are 80, 75, 70, 65 and 60 km from top to bottom.



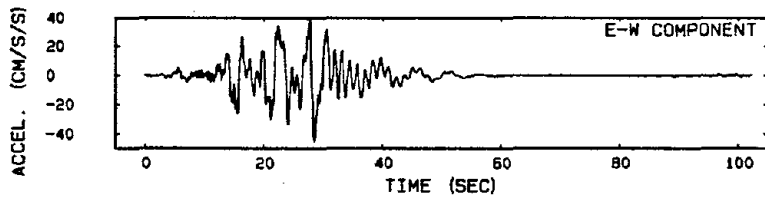
R: 55.0 PHI: 3.1 YM: 41.74  
 TAU: 0.7 VR: 1.9



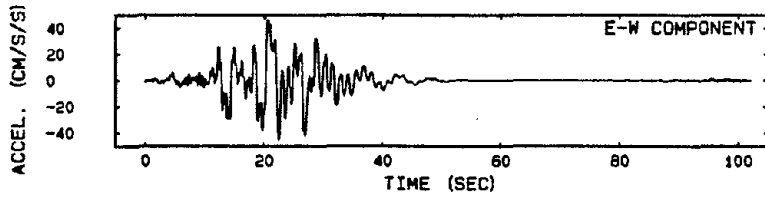
R: 50.0 PHI: 3.1 YM: 39.95  
 TAU: 0.7 VR: 1.9



R: 45.0 PHI: 3.1 YM: 45.56  
 TAU: 0.7 VR: 1.9

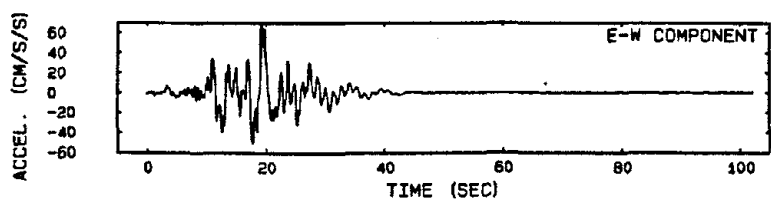


R: 40.0 PHI: 3.1 YM: 45.14  
 TAU: 0.7 VR: 1.9

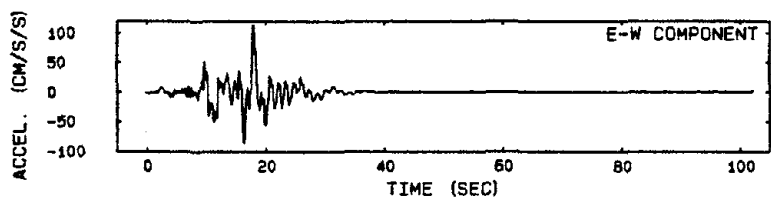


R: 35.0 PHI: 3.1 YM: 46.82  
 TAU: 0.7 VR: 1.9

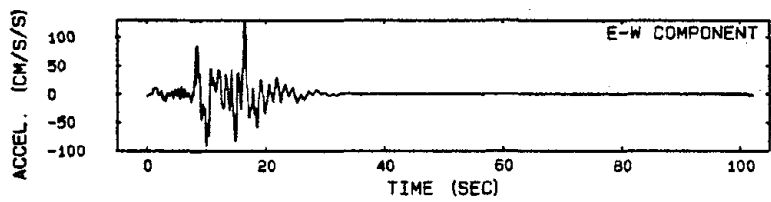
Figure 10. Simulated acceleration time histories for source HHR6 at sites along the direction away from the rupture propagation. Epicentral distances are 55, 50, 45, 40, and 35 km from top to bottom.



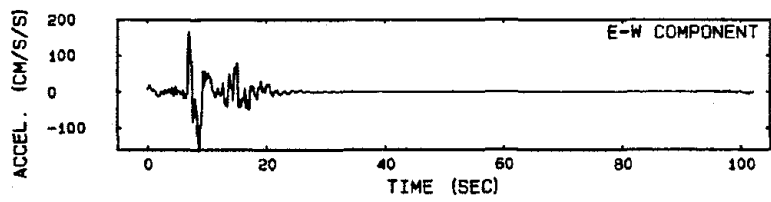
R: 30.0 PHI: 3.1 YM: 68.15  
 TAU: 0.7 VR: 1.9



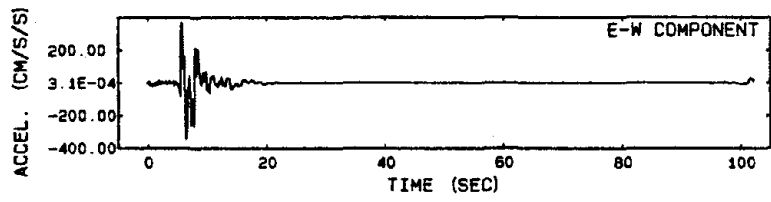
R: 25.0 PHI: 3.1 YM: 115.00  
 TAU: 0.7 VR: 1.9



R: 20.0 PHI: 3.1 YM: 128.94  
 TAU: 0.7 VR: 1.9



R: 15.0 PHI: 3.1 YM: 166.71  
 TAU: 0.7 VR: 1.9



R: 10.0 PHI: 3.1 YM: 373.14  
 TAU: 0.7 VR: 1.9

Figure 11. Simulated acceleration time histories for source HHR6 at sites along the direction away from rupture propagation. Epicentral distances are 30, 25, 20, 15, and 10 km from top to bottom.

us of the complexity of the superposition of waves arriving at a site at a given instant, and that there are inherent sources of variability in strong ground motion response which empirical ground motion models will never be able to capture.

Table 4 summarizes the results of regression analyses performed on the six data sets obtained through simulation. Three runs were made on each data set; one including only the R-dependence  $f_2(R)$  (equation 5), another adding in the directivity terms,  $f_2(R) + g_1(\phi)$ , and the third including the radiation pattern as well.

In each case above, adding the  $\phi$ -dependent terms reduces the standard error,  $\sigma_{\log}(y)$ , as systematic errors in the  $\phi$ -independent ground motion models are corrected by accounting for these azimuthal variations. The reduction in the standard deviation obtained by including the  $\phi$ -terms in these examples ranged from 30% to 40%. This reduction in standard deviation is significant at the 0.005 level, according to an F test. Thus we are 99.5% certain that the azimuthal terms belong in the model.

To observe this more closely, the residuals, or the observed values of  $\log_{10}(\text{pga})$  minus the predicted values, from the  $\phi$ -independent data set HHR5 are plotted as a function of azimuth (Figure 12). Data set HHR5 corresponds to a fault with bilateral rupture (approximately 40 km in the  $\phi = 0$  direction, and 18 km in the  $\phi = \pi$  direction), and so directivity focusing is anticipated primarily in the  $\phi = 0$  direction, and, to a lesser extent, in the  $\phi = \pi$  direction as well. In Figure 12, the residuals indicate that the  $\phi$ -independent ground motion model underestimates the actual ground motion amplitudes (positive residuals) near  $\phi = 0$  and  $\phi = \pi$ . At the same time, the variations in the residuals show a correspondence to the SH wave radiation pattern which is proportional to  $\cos(2\phi)$ . This agrees with the physical understanding that vertical strike-slip faults are more effective in generating SH waves than P-SV waves. Taking the directivity and SH radiation pattern into account in the regression model, the residuals in Figure 13 are obtained, and are plotted as a function of  $\phi$ . In the figure, the residuals are centered about the zero line. The standard deviations of the residuals corresponding to Figures 12 and 13 are 0.28 and 0.17 respectively.

Table 4

Summary of Regression Coefficients

Data Set	Model*	C <sub>1</sub>	C <sub>2</sub>	C <sub>3</sub>	C <sub>4</sub>	C <sub>5</sub>	C <sub>6</sub>	C <sub>7</sub>	$\sigma_{\log(y)}$
HHR0	1	1.330	-0.00255	-1.0	-2.27	0.73	0.057	-0.72	0.21
	2	0.234	-0.00255	-1.0	--	--	--	--	0.30
	3	0.456	-0.00255	-1.0	-0.49	0.16	--	--	0.27
HHR1	1	1.220	-0.00255	-1.0	-2.37	0.76	0.086	-0.72	0.22
	2	0.043	-0.00255	-1.0	--	--	--	--	0.32
	3	0.367	-0.00255	-1.0	-0.62	0.19	--	--	0.28
HHR2	1	0.938	-0.00255	-1.0	-1.73	0.55	-0.028	-0.40	0.20
	2	0.067	-0.00255	-1.0	--	--	--	--	0.29
	3	0.404	-0.00255	-1.0	--	--	--	--	0.22
HHR5	1	0.692	-0.00255	-1.0	-1.90	0.59	-0.065	-0.45	0.17
	2	-0.311	-0.00255	-1.0	--	--	--	--	0.28
	3	0.064	-0.00255	-1.0	-0.73	0.22	--	--	0.20
HHR6	1	0.159	-0.00255	-1.0	-2.03	0.61	0.095	-0.62	0.19
	2	0.450	-0.00255	-1.0	--	--	--	--	0.31
	3	0.869	-0.00255	-1.0	-0.52	0.11	--	--	0.25
HHR7	1	0.847	-0.00255	-1.0	-2.17	0.71	0.046	-0.69	0.21
	2	-0.189	-0.00255	-1.0	--	--	--	--	0.30
	3	-0.002	-0.00255	-1.0	-0.46	0.16	--	--	0.27

\* Model 1:  $y = C_1 + C_2R + C_3 \log R + C_4\phi + C_5\phi^2 + C_6|\sin 2\phi| + C_7|\cos 2\phi|$

2:  $y = C_1 + C_2R + C_3 \log R$

3:  $y = C_1 + C_2R + C_3 \log R + C_4\phi + C_5\phi^2$

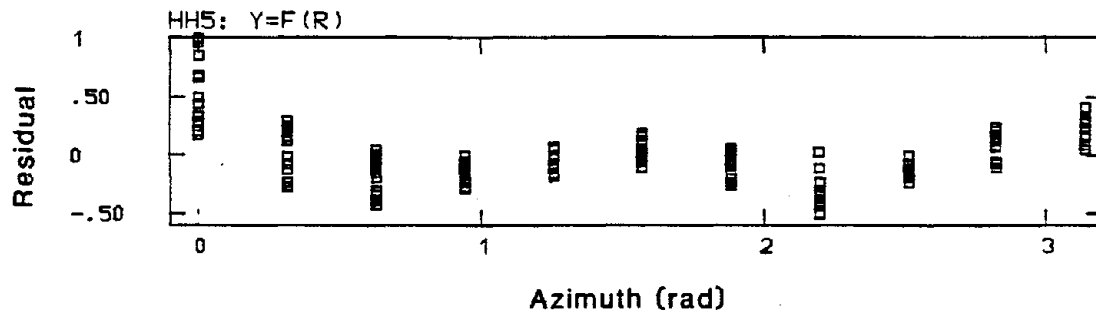


Figure 12. Residuals (observed minus predicted) for data set HHR5. Azimuthal terms are not considered in ground motion model.

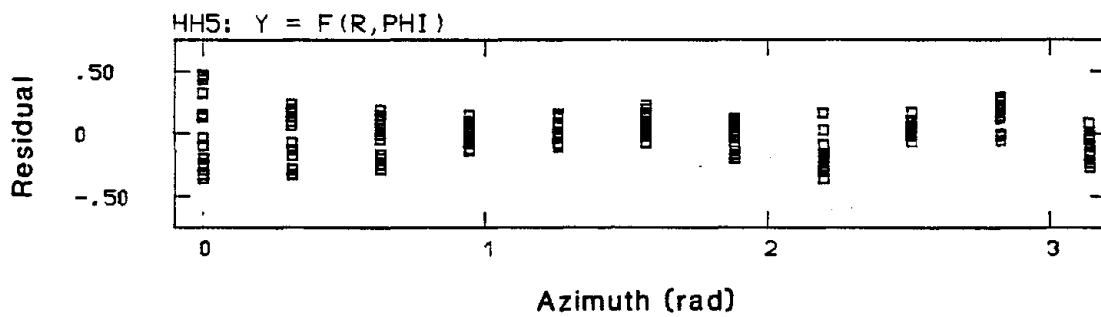


Figure 13. Residuals for data set HHR5 including azimuthal terms.

In both Figures 12 and 13, it appears that there is a greater variability in pga as  $\phi$  decreases. This is apparent in Figure 14, which shows the pga at each simulation node. Referring to Figure 14, one notices that for sites lying on the fault trace (the fault is buried at a depth of 7 km), each being the same distance from the fault, there is a great deal of variation in pga. At least a part of this is attributed to the non-uniformity of fault segments for this fault, as the potential for focusing of wave energy is related to the random length of each coherent rupture patch. At the same time, there is likely some error in the distance function  $f_2(R)$  for shorter source-site distances.

Finally, for HHR5, ground motion amplitudes are predicted for the  $\phi$ -independent and  $\phi$ -dependent cases and are compared for a source-site distance of 30 km in Figure 15. The  $\phi$ -independent case plots as a straight line, with the  $\phi$ -dependent curve exceeding the  $\phi$ -independent curve near the ends. By including directivity effects, the  $\phi$ -dependent model predicts a pga at  $\phi = 0$  which is four times greater than what is predicted by the  $\phi$ -independent model. This ratio is approximately two at  $\phi = \pi$ . Comparing the coefficients  $c_4$  and  $c_5$  in the cases when the radiation pattern is and is not included in the regression model, it appears that the radiation term  $\cos(2\phi)$  contributes in part to the fit of the radiation pattern. As an example, consider the regression analysis for HHR5. Neglecting the radiation pattern,  $c_4 = -0.731$  and  $c_5 = 0.225$ . This implies that the ratio of amplitudes at  $\phi = 0$  and  $\phi = \pi$  is 10 raised to the power  $(c_4\pi + c_5\pi^2) = 0.821$ . That is, amplitudes are approximately 18% less in the opposite direction of rupture propagation. However, when  $\cos(2\phi)$  is included, the ratio of amplitudes is 10 to the power  $(1.903(\pi) + .588(\pi)^2) = 0.668$ , i.e., amplitudes are 33% less in the  $\pi = \phi$  direction.

Figure 16 shows the distribution of peak ground accelerations for simulation HHR1 around a fault having rupture lengths of 21 km in the  $\phi = 0$  direction and 5 km in the  $\phi = \pi$  direction. Here, directivity focusing results in higher amplitudes in the  $\phi = 0$  and  $\phi = \pi$  direction than elsewhere. At the same time, the scaling associated with the SH-wave radiation pattern shows up very distinctly. The effect of radiation patterns is most important for

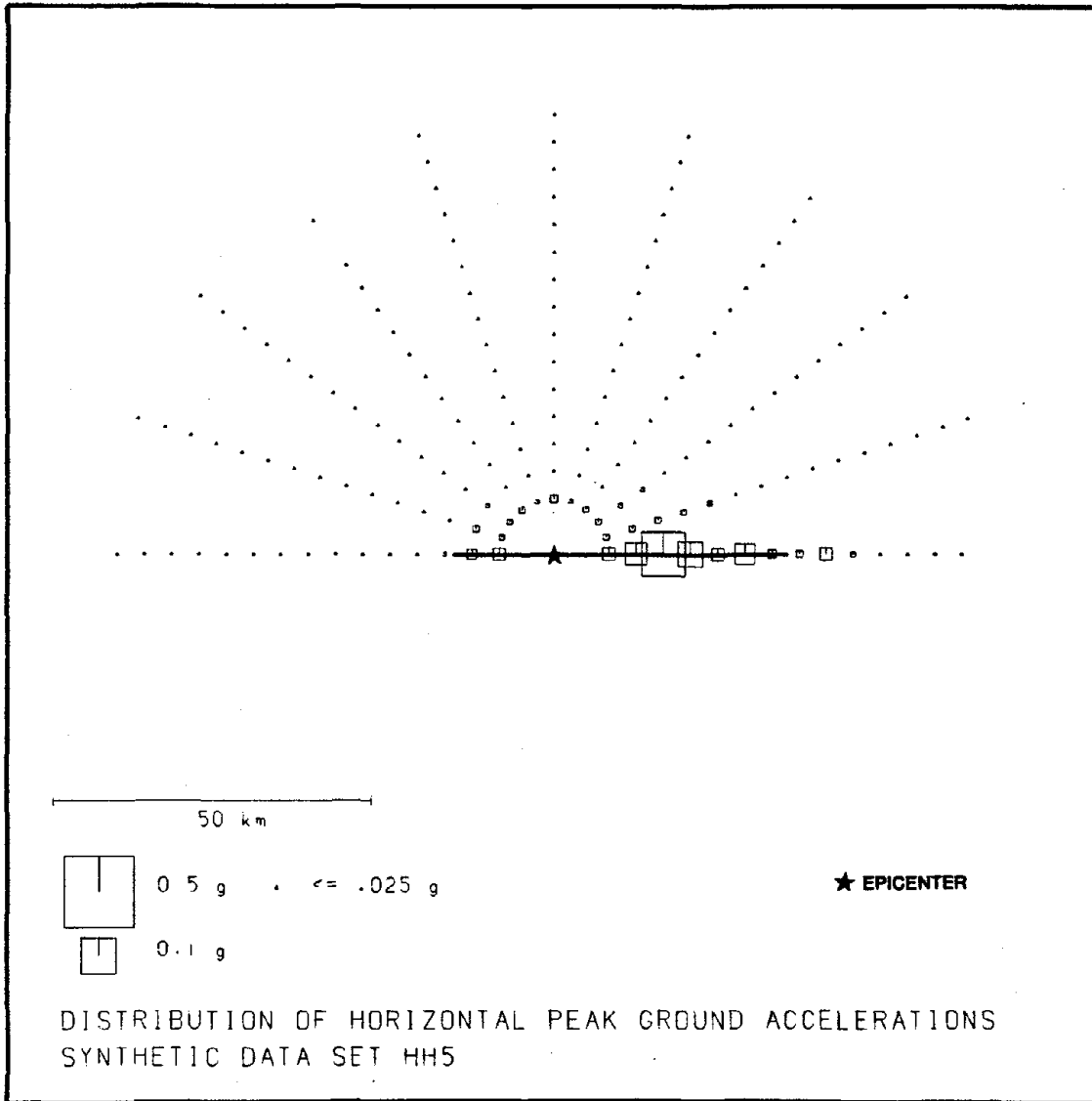


Figure 14. Distribution of horizontal peak ground accelerations for source HHR5.

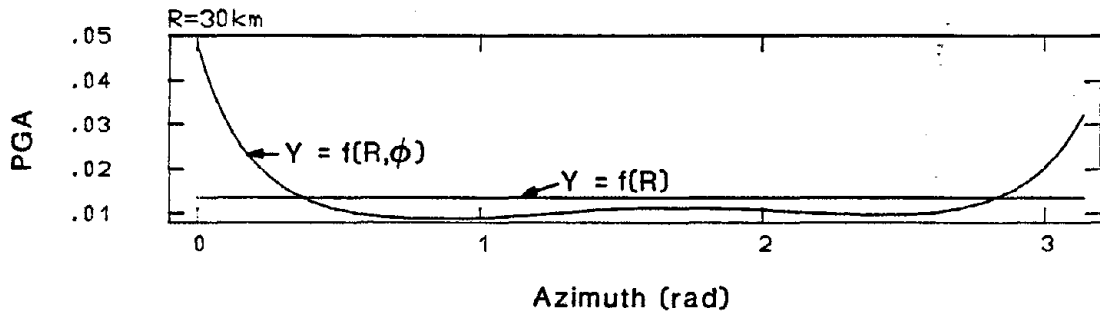


Figure 15. Predicted ground motion amplitudes as a function of azimuth, evaluated at  $R = 30$  km. Directivity focusing is evidenced through amplification near  $\phi = 0$ , and to a lesser degree at  $\phi = \pi$ . The SH-wave radiation pattern is apparent as well.

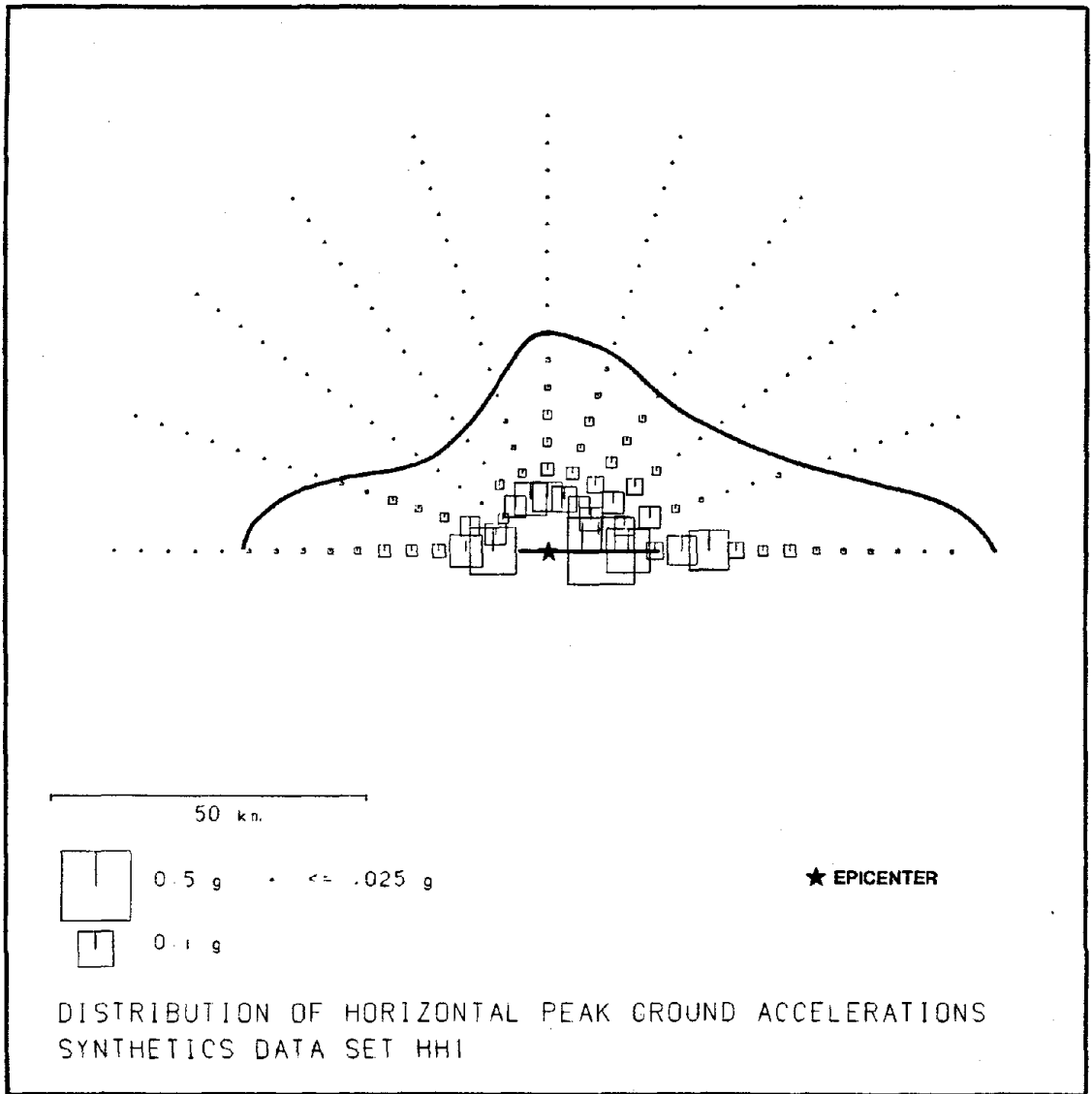


Figure 16. Distribution of horizontal peak ground accelerations for source HHR1. A contour has been superimposed on this data indicating the approximate locations where the pga drops below 0.025g.

faults with small rupture lengths; as the length of the rupturing surface becomes longer, the effects of radiation scaling tend to average out.

## 2.2 Discussion

The results of Section 2.1 highlight the importance of including azimuthal dependencies in the estimation of strong ground motion response. Both the peak amplitude of the response and the spatial distribution of the peak ground accelerations have been linked to the physical characteristics of the fault rupture process. Important also is the significant reduction in the errors associated with ground motion prediction obtained by incorporating azimuthal terms. This decrease in uncertainty has important implications when considering long return period events in seismic hazard estimation, as the evaluation of these low probability events is sensitive to the tails of the ground motion probability density function.

The use of synthetic accelerograms as an artificial data base has provided a mechanism by which theoretical considerations from the geosciences are included in the evaluation of ground motion response. Furthermore, this theoretical quantification of azimuthal effects allows the hazard analyst to account for such variations in a manner which is consistent with the fault rupture characteristics and earth structure for the region of interest.

### 3.0 AZIMUTHAL VARIATIONS IN OBSERVED STRONG GROUND MOTION RECORDS

In this section, the peak horizontal accelerations observed in two earthquakes are studied in an attempt to detect systematic variations in amplitudes associated with the azimuth of the recording site. For both events, the spatial distribution of peak ground accelerations is plotted with the location of the fault rupture. The closest distance to fault rupture and epicentral azimuth is calculated for each recording site, and regression analyses are performed to evaluate the impact of azimuthal effects in these events.

#### 3.1 Ground Motion Modeling for the 1984 Morgan Hill Earthquake

The April 24, 1984, Morgan Hill earthquake occurred on the Calaveras fault, east of San Jose, California. The surface wave magnitude  $M_s$  was 6.1; the body wave magnitude  $m_b$  was 5.7 (Bakun, et al. 1984). The determination of the focal mechanism for this event indicates right lateral strike slip motion, with a dip angle of 84 degrees (nearly vertical). The strike direction was N 33 W (Eaton, 1984). Figure 17, shows the location of the Calaveras fault that ruptured unilaterally from northwest to southeast for a distance of 25 km (estimated from the distribution of aftershocks). Figure 18 shows the locations of stations recording the main shock, with an indication of the horizontal peak ground acceleration. Where data were available on both horizontal components, the maximum value was selected.

This event exhibits evidence of constructive wave interference, producing larger amplitudes to the southeast, and lower amplitudes to the northwest. A notable case is the 1.29g acceleration recorded at Coyote Lake. This is attributed to a double-source mechanism (Abrahamson and Darragh, 1985), where waves leaving the first source aligned with those produced by an energetic second source, located approximately 17 km southeast of the epicenter. Abrahamson and Darragh point out that peak accelerations are approximately three times larger in the direction of rupture propagation than in the back azimuth.

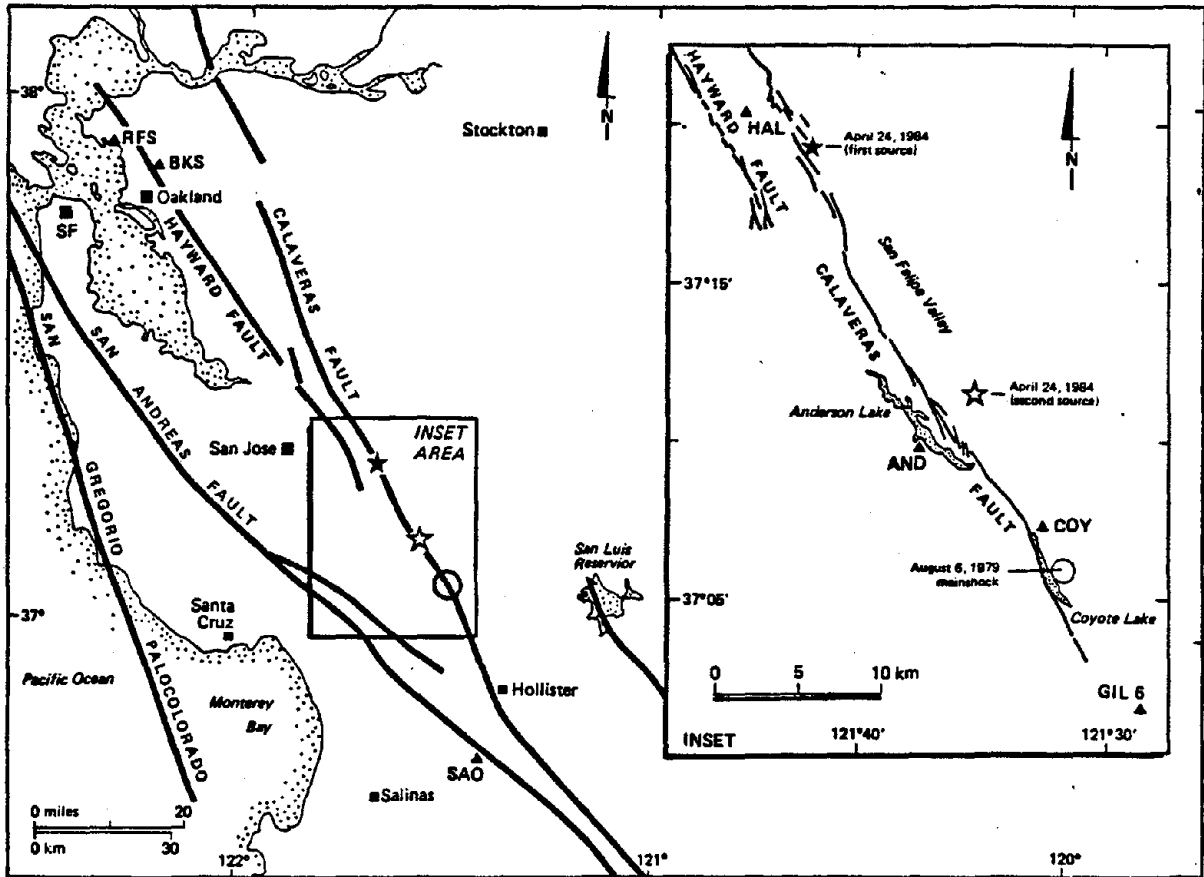


Figure 17. Location of the Calaveras fault zone and the main and secondary source epicenters (from Abrahamson and Darragh, 1985).

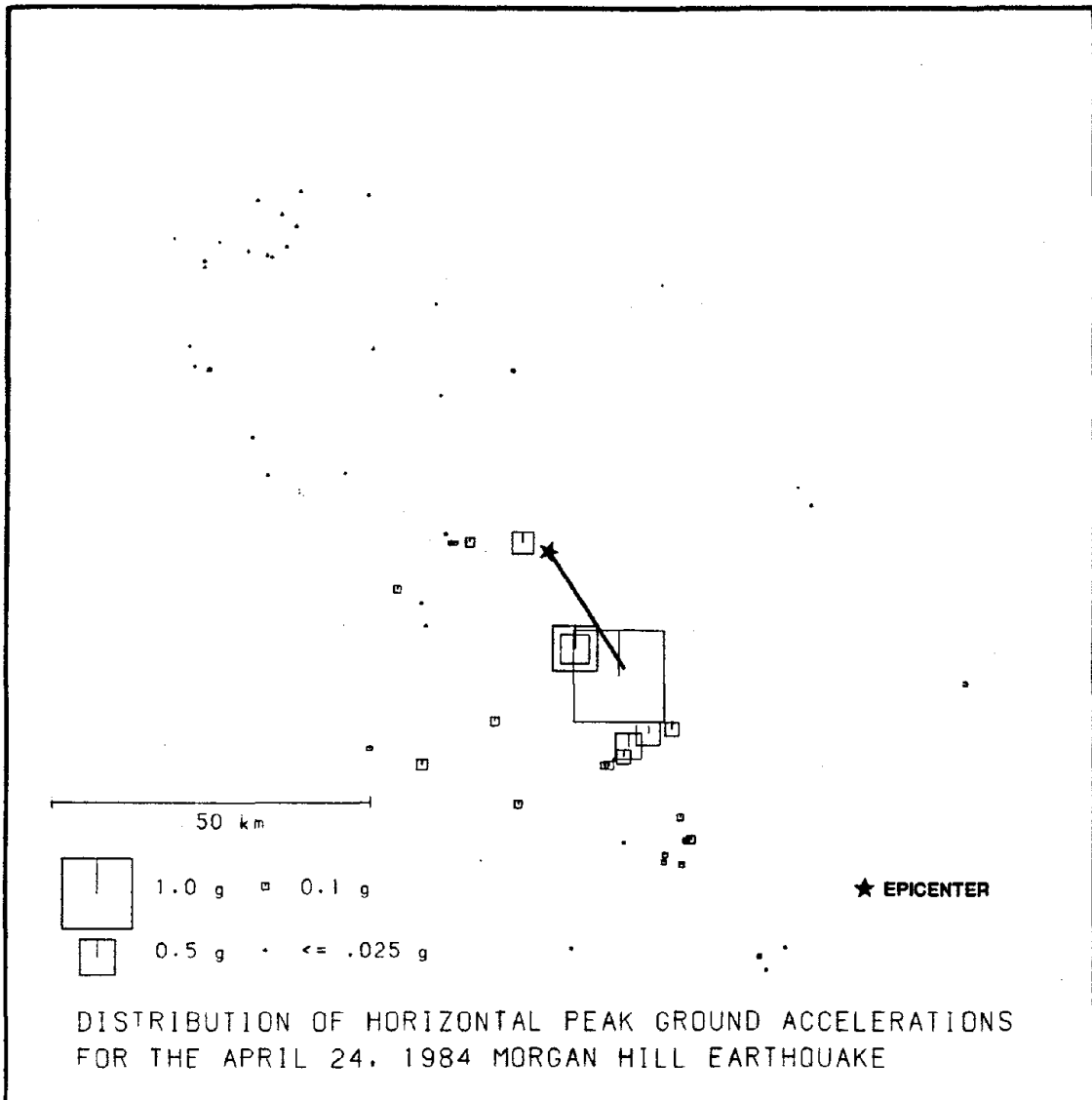


Figure 18. Distribution of horizontal peak ground accelerations for the April 24, 1984 Morgan Hill earthquake.

The ground motion relationship used to account for the azimuthal variations in this event is given in equation 11. Table 5 compares the results of the regression analysis using this model with the results of using the  $\phi$ -independent model.

**Table 5**  
**Regression Coefficients for Morgan Hill Data Set**

Model	$c_1$	$c_2$	$c_3$	$c_4$	$c_5$	$c_6$	$c_7$	$\sigma_{\log(y)}$
1	.371	-.00255	-1.0	--	--	--	--	.28
2	.558	-.00255	-1.0	-.184	.028	--	--	.26
3	.226	-.00255	-1.0	.400	-.151	.068	.222	.26

Model 1:  $y_1 = c_1 + c_2R + c_3 \log_{10}(R)$

Model 2:  $y_2 = c_1 + c_2R + c_3 \log_{10}(R) + c_4\phi + c_5\phi^2$

Model 3:  $y_3 = c_1 + c_2R + c_3 \log_{10}(R) + c_4\phi + c_5\phi^2 + c_6$   
 $| \sin 2\phi | + c_7 | \cos 2\phi |$

The residuals are plotted in Figure 19 for Model 1. A trend is observed, although subject to much scatter, in which the residuals go from positive to negative as  $\phi$  goes from 0 to  $\pi$ , indicating that the observed amplitudes in the direction of rupture propagation are generally higher than what the  $\phi$ -independent ground motion model predicts, and are generally lower in the back-azimuth. There is no observable evidence of scaling due to radiation pattern in these data.

There was only a slight decrease, from 0.28 to 0.26, in the standard error of the residual by adding the  $\phi$  and  $\phi^2$  terms in Model 2, and virtually no decrease when the  $\sin 2\phi$  and  $\cos 2\phi$  terms were added. Therefore, given the number of observed data, it is not possible to state with high confidence that the data support the azimuthal dependencies included in Models 2 and 3 (especially for Model 3).

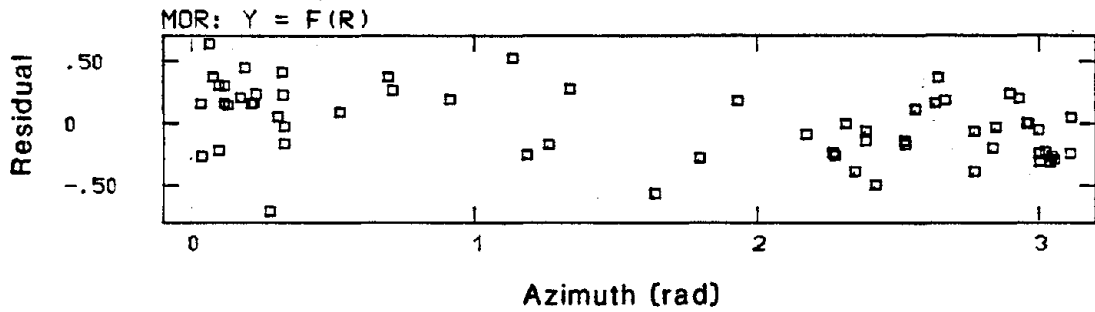


Figure 19. Residuals (observed minus predicted) for the Morgan Hill event neglecting azimuthal terms in the ground motion model. Observed data generally exceeds the predicted values near  $\phi = 0$ , and are generally less than the predicted values near  $\phi = \pi$

The regression curves for the  $\phi$ -independent model (Model 1) and the  $\phi$ -dependent model (Model 2) are plotted for a source-site distance of 30 km in Figure 20. The monotonic decrease in pga is anticipated for the unilateral fault rupture for this event. The  $\phi$ -dependent model predicts amplitudes which are approximately 50% greater than the  $\phi$ -independent model at  $\phi = 0$  and amplitudes which are approximately 25% less in the  $\phi = \pi$  direction.

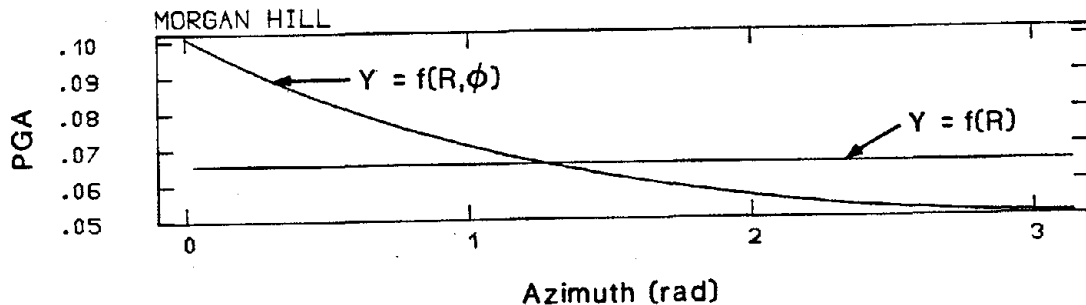


Figure 20. Ground motion model for Morgan Hill event including azimuthal terms, evaluated at  $R = 30$  km. This  $\phi$ -dependent model predicts amplitudes which are 50% greater than those for the  $\phi$ -independent model at  $\phi = 0$ , and predicts amplitudes which are 25% less at  $\phi = \pi$ .

### 3.2 Ground Motion Modeling for the 1980 Campania-Lucania Earthquake

The November 23, 1980, Campania-Lucania earthquake in southern Italy had a 6.5 Richter magnitude (Barnardi, 1981), and triggered 21 accelerometers. The fault dislocation was primarily normal (dip angle =  $75^\circ$ ) with a small strike component. The hypocenter was approximately 17 km deep. Figure 21 shows the spatial distribution of peak horizontal accelerations representing the maximum amplitude of the two horizontal components.

This event is of particular interest because the observed pga's show a strong correlation with the radiation pattern for a normal fault. The radiation pattern for this type of fault is proportional to  $|\sin\phi|^*$  and  $|\cos\phi|$ , so the function  $g_2(\phi)$  in equation 9 is used in the regression analyses, the results of which are given in Table 6. The reduction in standard deviation by adding azimuthal variation is significant at the 0.1 level, according to an F test.

Figure 22 shows a plot of the residuals in the  $\phi$ -independent model (Model 1) as a function of  $\phi$ . Here the amplitudes are overestimated in the  $\phi = 0$  and  $\phi = \pi$  directions (where the radiation pattern amplitude is small), and are underestimated near  $\phi = \pi/2$ .

In Table 6, it is noted that the quadratic function representing azimuthal variations does just as good a job in predicting the amplitude as the  $|\sin\phi|$  and  $|\cos\phi|$  terms do, as it assumes a shape which is concave downward, similar to  $|\sin\phi|$ . A comparison of the  $\phi$ -independent and  $\phi$ -dependent ground motion models (1 and 3) evaluated at  $R = 30$  km, is shown in Figure 21. This curve is distorted somewhat (the dip at  $\phi = \pi/2$ ) as a result of the relatively large coefficient for  $|\cos\phi|$  and the fact that the function  $\exp(\sin\phi)$  is used to fit the data. Omitting the  $|\cos\phi|$  term in the regression analysis, in order to obtain a symmetric function, the ground motion model in Figure 24 is computed. The standard deviation is increased somewhat (to 0.28), reducing the confidence in this model to below 90%, the confidence level obtained when the  $|\cos\phi|$  term is retained.

\* Because the dip angle is large ( $75^\circ$ ), the radiation pattern will be dominated by the  $|\sin\phi|$  term.

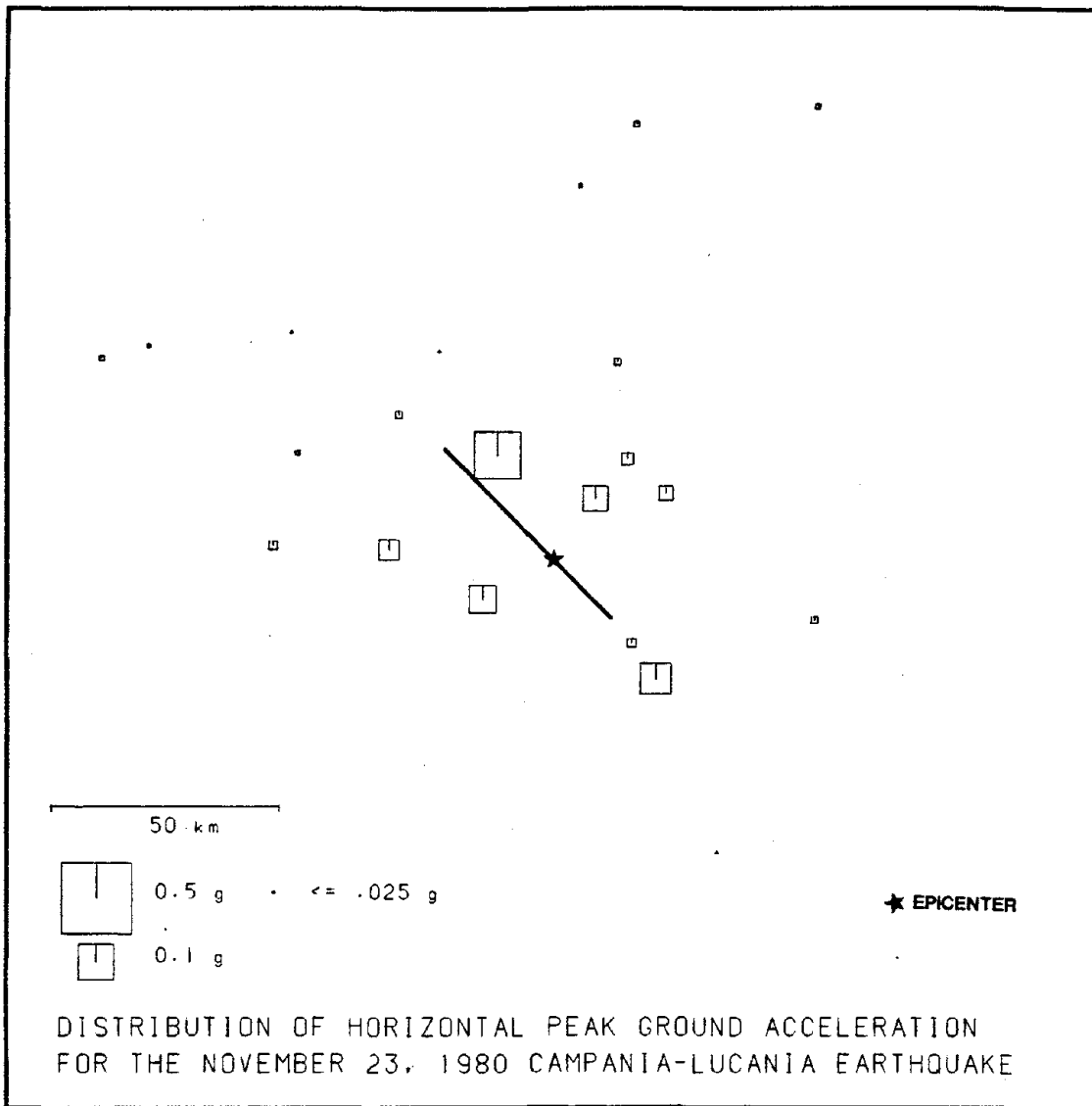


Figure 21. Distribution of horizontal peak ground accelerations for the Campania-Lucania earthquake.

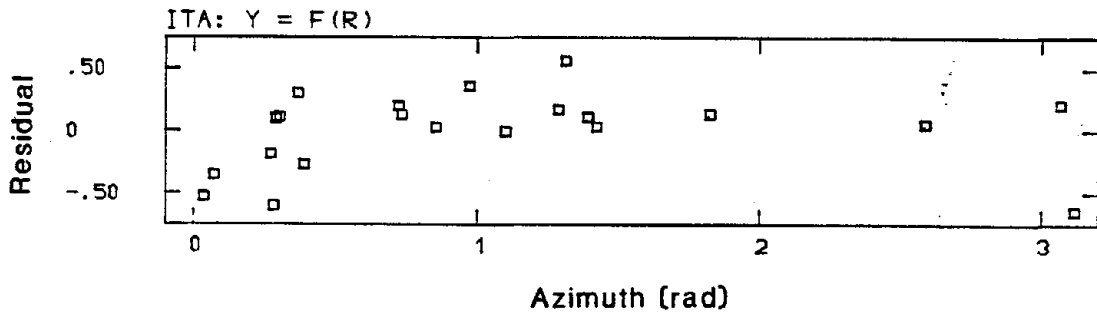


Figure 22. Residuals (observed minus predicted) for the Campania-Lucania event, neglecting azimuthal terms. Note the systematic trend of over-estimation of amplitude.

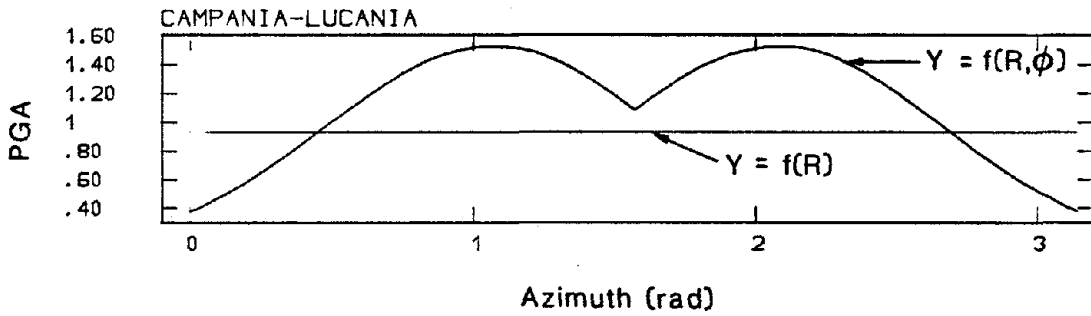


Figure 23. Predicted ground motion amplitudes for Campania-Lucania earthquake as a function of azimuth, evaluated at  $R = 30$  km. While this curve gives the lowest mean square residual, the dip near  $\phi = \pi/2$  illustrates a shortcoming in the azimuthal terms used to fit the radiation pattern.

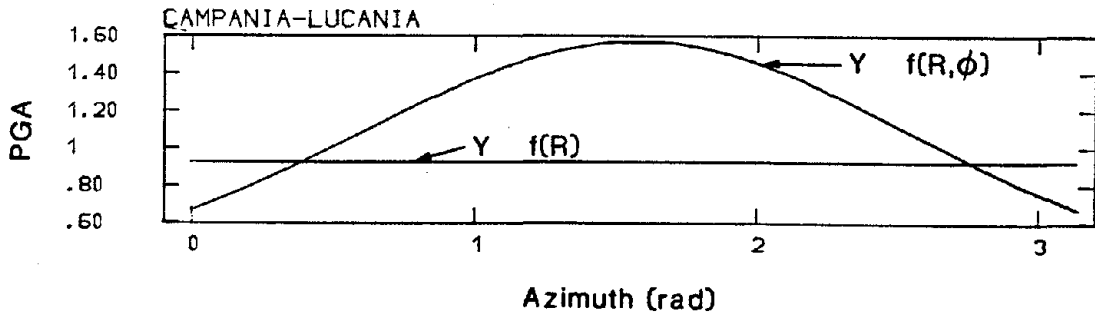


Figure 24. Predicted ground motion amplitudes for Campania-Lucania earthquake, retaining only  $\sin\phi$  for the radiation pattern function, evaluated at  $R = 30$  km.

**Table 6**  
**Regression Coefficients for the Campania-Lucania Data Set**

Model	$c_1$	$c_2$	$c_3$	$c_4$	$c_5$	$c_6$	$c_7$	$\sigma_{\log(y)}$
1	1.52	-.00255	-1.0	--	--	--	--	.33
2	1.12	-.00255	-1.0	1.152	.527	--	--	.25
3	0.55	-.00255	-1.0	--	--	1.04	0.58	.25

Model 1:  $y_1 = c_1 + c_2R + c_3 \log_{10}(R)$

Model 2:  $y_2 = c_1 + c_2R + c_3 \log_{10}(R) + c_4\phi + c_5\phi^2$

Model 3:  $y_3 = c_1 + c_2R + c_3 \log_{10}(R) + c_6 |\sin\phi| + c_7 |\cos\phi|$

### 3.3 Discussion

In both the Morgan Hill and Campania-Lucania data sets, a reduction in the uncertainty in the ground motion prediction models was achieved, although the confidence levels for both are below 90%. This does not mean that the azimuthal terms introduced in the ground motion models are invalid, but that there are not enough data to pass statistical significance tests at high confidence levels.

However, the azimuthal terms were easily justified, with 99.5% confidence, in synthetic data with sufficient samples (Section 2). A more reliable method for evaluating azimuthal variations in observed strong motion data is described by Boatwright and Boore (1982), where data from two of the Livermore earthquakes during January of 1980 are analyzed. In these events, the direction of unilateral rupture propagation reversed; that is, in the January 24 event, the rupture propagated from north to south, and in the January 27 event, from south to north. This allowed Boatwright and Boore to analyze the ratio of peak ground accelerations at each recording station for the two events, and in effect, filter out the effects of local site conditions and propagation effects by assuming that such factors affect the observed response at a given station in a similar manner.

#### 4.0 STRONG GROUND MOTION ESTIMATION FOR SEISMIC HAZARD ANALYSIS

The examples in Section 3 reflect the difficulties in quantifying azimuthal dependencies from observed ground motion data. While the correlations obtained are consistent with a physical understanding of fault rupture processes, the data were not sufficient to allow high confidence conclusions that azimuthal effects were the cause for the variability in the observed data. However, the azimuthal terms always improved the fit, whether statistically significant or not. In Section 2, on the other hand, it was found that theoretically, these azimuthal variations are extremely important in estimating strong ground motion response. Faced with the need to provide estimates of strong ground motion response for seismic hazard mapping, one must utilize all sources of information, including the observed (although scattered) data, as well as theoretical information.

#### 4.1 Combination of Observed and Theoretical Information

The information typically required by the seismic hazard analyst is the mean and variance of the ground motion response,  $\bar{y} = \overline{\log_{10}(\text{pga})}$  and  $\sigma_{\log_{10}(\text{pga})}^2$ , given the magnitude, distance, and now, azimuth of a site. These two parameters can be used to define the normal probability density function  $f_{y|M,R,\phi}(y|m,r,\phi)$ . Bayesian estimates of the mean and variance are obtained as a combination of the observed and theoretical information on ground motion response (see Benjamin and Cornell, 1970; Schoof, 1984). The prior distribution on the mean value of the ground motion response,  $\bar{y}^*$ , is obtained from regression analyses performed on data from synthetic acceleration time histories, as in Section 2. Since this information is linked to specific earth structure and fault rupture characteristics, several different prior distributions may be developed, wherein unilateral rupture propagation is considered in one, bilateral rupture in another, etc., and included in the hazard analysis. The prior variance,  $\sigma^{*2}$  is obtained as the variance of the residuals. The prior distribution of the mean ground motion response can be assumed normally distributed with mean  $\bar{y}^*$  and variance  $\sigma^{*2}$  :

$$f_Y^*(y) = N(\bar{y}^*, \sigma^{*2}) \quad (12)$$

where  $\bar{y}^* = f_1(m) + f_2(R) + f_3(\phi)$

and  $f_3(\phi)$  depends on the azimuthal terms being considered.

Observed data are used to define the likelihood function and are, for convenience,† assumed to be normally distributed with known variance,  $s^2$ . The mean value of the data is described using  $\bar{y} = f(M,R,\phi)$  from the observed data, as in Section 3. Since the response data mean and prior mean are both normal, the posterior distribution on the mean ground motion is a weighted average of the data mean and prior mean:

$$\bar{y}^{**} = \frac{\frac{\bar{y}^*}{\sigma^{*2}} + \frac{\bar{y}}{(s^2/n)}}{\frac{1}{\sigma^{*2}} + \frac{1}{(s^2/n)}} \quad (13)$$

where  $n$  is the number of observed data.

The posterior variance is:

$$\sigma^{**2} = \left[ \frac{1}{\frac{1}{\sigma^{*2}} + \frac{1}{(s^2/n)}} \right] \quad (14)$$

The Bayesian distribution on the ground motion parameter  $y$  is

$$f_{Y|M,R,\phi}(y|m,r,\phi) = [2\pi (s^2 + \sigma^{**2})]^{-1/2} \exp[-1/2 \frac{(\bar{y}-y^{**})^2}{(s^2 + \sigma^{**2})}] \quad (15)$$

† If the prior and data are both normally distributed, the posterior distribution will also be normal. (See Raiffa and Schlaifer, 1961, for conjugate distributions).

The following example illustrates the development of the posterior distribution on the mean ground motion response considering unilateral rupture propagation as observed in the Morgan Hill earthquake. Prior information on the mean value of peak ground acceleration given an event size, distance, and azimuth is obtained from the analysis of data set HHR5 from Section 2. This assumes that the ground motion scaling associated with azimuthal effects for the Morgan Hill area are similar to those synthesized using the Imperial Valley earth structure. The prior mean is shown in equation 16.

$$\begin{aligned} \bar{y}^* = & 0.692 - .00255 + R - \log_{10}(R) - 1.903\phi + 0.588\phi^2 \\ & -0.065 |\sin 2\phi| - 0.454 |\cos 2\phi| \end{aligned} \quad (16)$$

The function  $\bar{y}^*$  is scaled such that the expected peak ground acceleration at any azimuth is equal for the  $\phi$ -dependent and  $\phi$ -independent ground motion models in order to retain only the azimuthal information contained in the synthetics. That is,

$$\frac{1}{\pi} \int_0^\pi f_1(R) d\phi = \frac{1}{\pi} \int_0^\pi f_1^*(R) + g_1^*(\phi) + g_2^*(\phi) d\phi$$

This is achieved by replacing  $c_1$  ( $= 0.692$ ) in equation 16 with 1.432. The prior mean becomes

$$\begin{aligned} \bar{y}^* = & 1.432 - 0.00255R - \log_{10}(R) - 1.903 \phi + 0.588\phi^2 \\ & -0.065 |\sin\phi| - 0.454 |\cos\phi| \end{aligned} \quad (17)$$

The prior variance is  $\sigma^{*2} = (0.17)^2 = 0.029$ . The sample mean  $\bar{y}$  is

$$\bar{y} = 0.558 - 0.00255R - \log_{10}d(R) - 0.184 \phi + 0.028 \phi^2 \quad (18)$$

and the assumed sample variance,  $s^2$  is  $(0.26)^2 = 0.068$ .† The resulting posterior mean and variance are:

$$\bar{y}^{**} = 0.588 - 0.00255R - \log_{10}R - 0.247 \phi + 0.048 \phi^2 - 0.002 |\sin 2\phi| - 0.017 |\cos 2\phi| \quad (19)$$

and

$$\sigma^{**2} = 0.0011$$

and  $\sigma^{**} = 0.0324$ . In this example,  $n$ , the number of observed data, is 62. As other data sets exhibiting unilateral fault rupture become available, these would be used to refine the estimates of the sample mean. The expected value of pga is plotted as a function of azimuth in Figure 25, and is compared with the  $\phi$ -independent response amplitude obtained in Section 3.1.

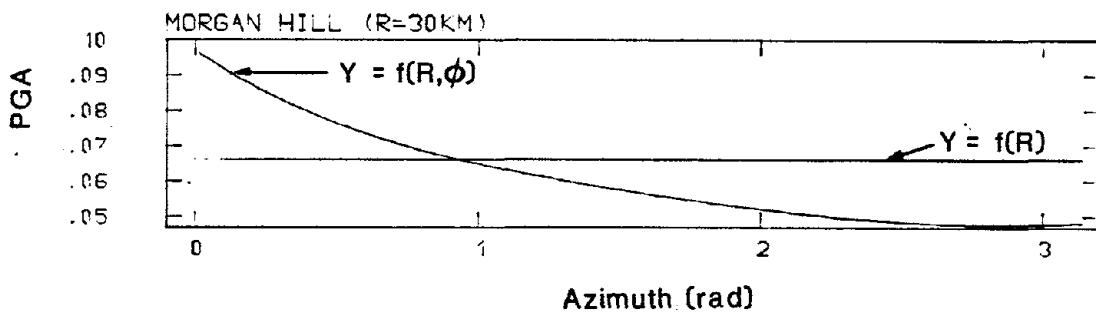


Figure 25. Predicted ground motion amplitudes for Morgan Hill example using the Bayesian distribution for the peak ground acceleration. This curve, evaluated at  $R = 30$  km, is based on theoretical information from the simulated HHR5 and on data observed in the Morgan Hill earthquake.

The Bayesian distribution of  $y = \log_{10}(\text{pga})$  is given in equation 20.

$$f_{Y|M,R,\phi}(y|m,r,\phi) = 1.523 \exp\left[-\frac{1}{2} \frac{(y - \bar{y}^{**})^2}{0.0687}\right] \quad (20)$$

where  $\sigma \log_{10}(y) = 0.262$ . This probability density function is integrated to obtain the probability that  $y$  lies within a given range. Specifically, it is of interest in seismic hazard analysis to know the probability that  $y$  is less than a given level  $y_0$ :

† This value of  $s$  is taken from Joyner and Boore.

$$P[y < y_0] = \int_{-\infty}^{y_0} 1.523 \exp \left[ -\frac{1}{2} \frac{(y - \bar{y}^{**})^2}{0.0687} \right] dy \quad (21)$$

The cumulative distribution function in equation 21 is a result of utilizing both subjective information (theoretical information from the analysis of synthetic time histories) and objective (observed) data. As such, it represents a more complete description of the random variable  $y$  and provides improved estimates of the seismic hazard at a site. In Section 4.2, a hazard analysis is performed using the above Bayesian distribution on  $y$  given an event size, the source-to-site distance, and the epicentral azimuth.

To summarize, probabilistic ground motion models are obtained by developing the prior distribution on the mean value of the ground motion response parameter using the synthetic acceleration time histories. A large ensemble of pseudo-observations is generated for a particular earth structure, and the ground motion response,  $pga$ , is evaluated as a function of the event size, source-site distance, and epicentral azimuth. That is,  $y^* = f(M, R, \phi)$ . The term  $y^*$  is the mean value of the response for the specified values of  $M$ ,  $R$ , and  $\phi$ , and is taken to be the prior mean of the ground motion response parameter. The prior variance,  $\sigma^{*2}$  is defined by the residuals of the synthetic observations with respect to  $y^*$ .

Observed data, if they exist, are used to update the prior information on the mean value of the response. The mean value of the data is represented by a different function relating the ground motion response to the same, or different, independent variables. The variance, which in this development is assumed to be known, can be taken as the variance obtained in global ground motion studies, which include uncertainties in propagation path effects, local variations in amplitude, etc.

The posterior mean and variance of the expected ground motion response are calculated as shown in equations 13 and 14. These, in addition to the inherent variability of the data are combined to give the Bayesian distribution of the ground motion response parameter (equation 15). This distribution will always have a variance which is greater than (or in the limit, equal to) the inherent variability in the ground motion response. However, the mean value can change dramatically, as in the case when azimuthal terms are added to the ground motion model.

It is re-emphasized that observed data are not required to obtain the Bayesian distribution on the ground motion response parameters. If no applicable observed data are available, the posterior distribution can be taken to be equal to the prior. At the other extreme, a diffuse, or non-informative prior can be assumed, wherein the observed data carry all the weight in specifying the posterior distribution.

#### 4.2 Hazard Analysis for the Morgan Hill Region

To test the impact of including azimuthal terms in the ground motion model for peak ground acceleration, the seismic hazard is evaluated for the Morgan Hill region assuming that a 30 km rupture occurs on the Calaveras fault once per year. The fault rupture is assumed to propagate unilaterally, but can proceed to either the northwest or the southeast with equal probability. Further, the 30 km rupture segment can occur along any portion of the fault with equal probability.

The pga's corresponding to 100-year return period are given for the  $\phi$ -independent and  $\phi$ -dependent ground motion models in Table 7. The location of each site, and the ratio of  $pga_{100}$  for the  $\phi$ -dependent and  $\phi$ -independent models are shown in Figure 26. It is noted at S1, which is 30 km from the fault, that the  $\phi$ -dependent model indicates higher accelerations, as anticipated, because the rupture can propagate directly toward the site. Figures 27 and 28 show the exceedence probabilities and return period curves for site S1 for both the ground motion models. Note that in Figure 28, the difference in pga's increases as the return period increases. At station S2, still 30 km away from the fault, the  $\phi$ -dependent model indicates much lower (nearly 50%) accelerations than the model which neglects azimuthal terms. Moving to stations along a normal to the midpoint of the fault, the  $\phi$ -independent ground motion model consistently overestimates the peak ground accelerations when directivity focusing is important. This seems to become more pronounced at sites further away from the fault trace. The ratio of  $pga_{100}$  for the  $\phi$ -dependent model to  $pga_{100}$  for the  $\phi$ -independent model decreases from 0.88 to 0.75 as the source-site distance increases from 20 km to 50 km. In a case not shown in Table 7, a site 5 km from the fault midpoint

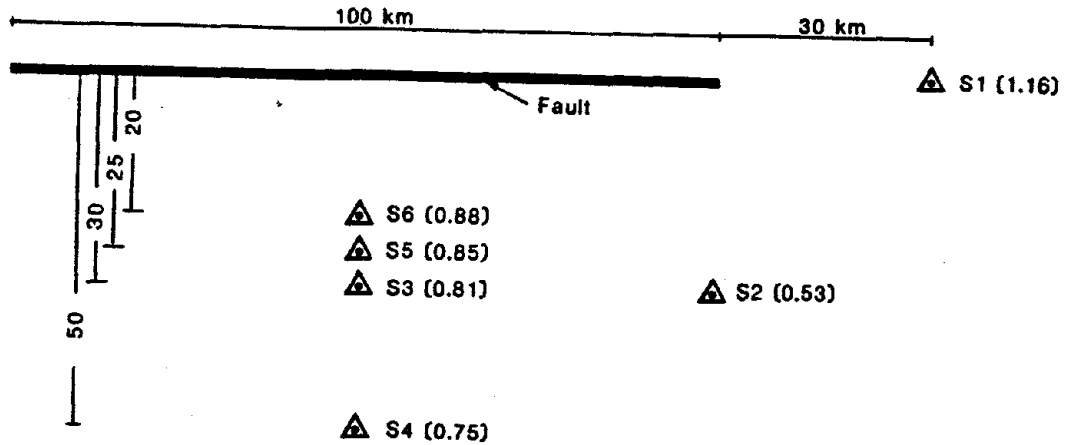


Figure 26. Comparison of 100-year peak ground accelerations at sites SS1-SS6 using  $\phi$ -dependent and  $\phi$ -independent ground motion models. The number in parentheses is the ratio of  $pga_{100}$  for the  $\phi$ -dependent model to  $pga_{100}$  for the  $\phi$ -independent model. The  $\phi$ -dependent model yields hazard estimates which are larger close to the fault than the  $\phi$ -independent model. At larger distances, the  $\phi$ -independent model predicts higher ground motion response.

has a ratio of pga's equal 1.05. It is anticipated that on the fault trace, the  $\phi$ -dependent model will always indicate an increase over the  $\phi$ -independent model similar to that for site S1.

This example shows how the channeling of wave energy along the fault results in higher seismic hazard at the fault ends, but a much lower hazard perpendicular to the fault. This will naturally have a great impact on seismic hazard mapping which, to date, does not account for the focusing potential of seismic waves.

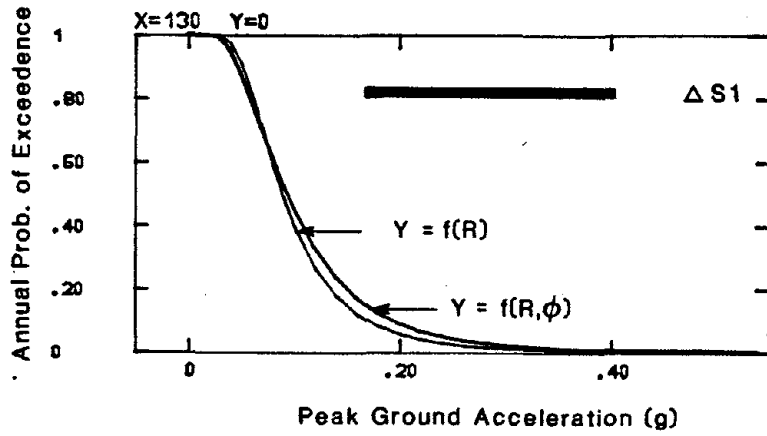


Figure 27. Comparison of exceedence probabilities at site SS1 for the  $\phi$ -dependent and  $\phi$ -independent ground motion models as a function of peak ground acceleration.

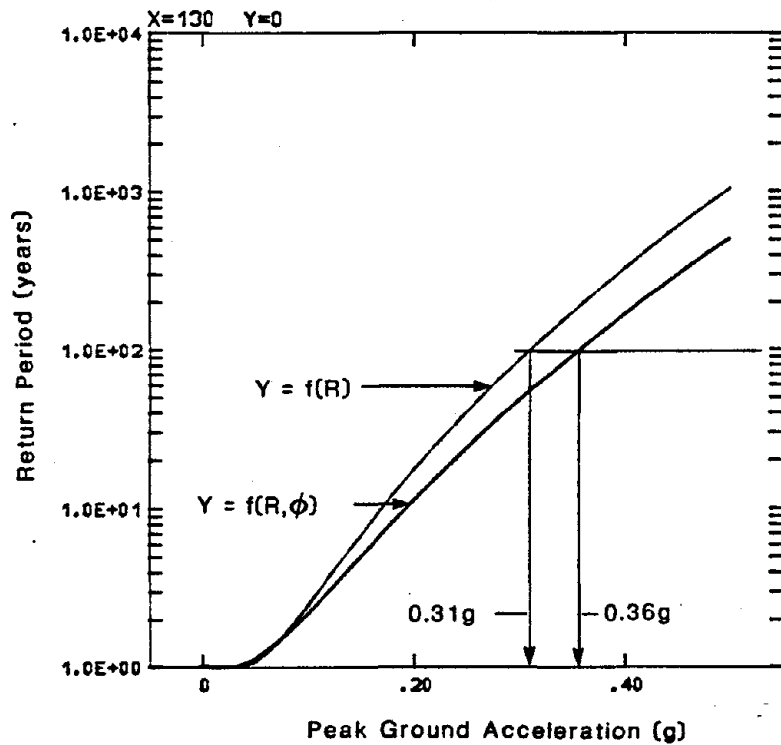


Figure 28. Comparison of return periods at site SS1 for  $\phi$ -dependent and  $\phi$ -independent models as a function of peak ground acceleration.

Table 7

Comparison of 100-Year Return Period Peak Ground Accelerations  
for  $\phi$ -Independent and  $\phi$ -Dependent Ground Motion Models

Site	R(km)	$\phi$ -Independent pga <sub>100</sub> (g)	$\phi$ -Dependent pga <sub>100</sub> (g)	Ratio $\phi$ -Dependent/ $\phi$ Independent
S1	30	.36	.31	1.16
S2	30	.36	.19	0.53
S3	30	.43	.35	0.81
S4	50	.24	.18	0.75
S5	25	.52	.44	0.85
S6	20	.65	.57	0.88

#### 4.3 Discussion

In an actual hazard analysis, several different ground motion models representing different rupture scenarios should be considered. For example, one model representing unilateral rupture propagation and directivity focusing, another considering bilateral rupture, and a third which does not include directivity focusing effects might be utilized. In such a case, it would be necessary to assess the probability that each of these scenarios would occur for a given earthquake. The lack of reliable observations of directivity focusing at this point precludes such assessments on a relative frequency basis, and consequently, subjective assessments (engineering judgment) would have to provide these probabilities.

## 5.0 RESULTS AND CONCLUSIONS

In this study, the variations in strong ground motion response (pga) associated with azimuthal effects have been evaluated on the basis of two distinct sources of information. First, a realistic source rupture/wave propagation model was used to simulate nearly 1000 time histories representing six different rupture processes. These served as an artificial data base with which to quantify the scaling of peak ground accelerations as functions of the seismic radiation pattern and directivity focusing potential. This scaling was then incorporated into the classical form of ground motion models which include functions of magnitude and source-site distance by adding a quadratic function of azimuth (to account for directivity) and harmonic functions of azimuth (to account for radiation pattern). The predictive capability of this refined model is evidenced by the dramatic decrease in the residuals obtained as the difference between the actual peak ground accelerations observed in the simulations and the values predicted by the new ground motion model. The standard deviation of the residuals was 30% to 40% lower when the azimuthal terms were considered, a difference that is statistically significant at the 0.005 level.

The same methods used to evaluate the functional relationships between peak ground acceleration and the azimuth of an observation point for the simulated acceleration records were used to correlate the observed pga's with the station azimuth in two actual earthquakes. These correlations did not result in the drastic, highly significant decrease in standard deviations obtained in the simulations, although reductions of 8% and 25% were realized. In both cases, the azimuthal functions obtained through regression analysis were indicative of the source rupture characteristics observed in each earthquake.

In order to effectively utilize the results from both the theoretical simulations and those based on strong ground motion observations, a Bayesian probability model was developed which will allow one to evaluate the mean value and variance of the ground motion response as a function of the size of an earthquake, the source-to-site distance, and the epicentral azimuth. Either theoretical information, observed data, or both can be used to evaluate the expected ground motion response.

An example was presented in which both theoretical information and observed data were used to characterize the strong ground motion response for a fault exhibiting directivity focusing. It was found that at sites near the ends of a fault, the focusing of wave energy resulted in 100-year return period accelerations that were 16% greater than what would have been predicted ignoring the azimuthal terms. For sites adjacent to the fault trace, directivity focusing produces 100-year pga's which exceed the classical estimates by approximately 10%. However, as the source-site distance for these sites increases beyond approximately 10 km, the classical ground motion models yield 100-year pga's that exceed those obtained by including directivity. At a distance of one rupture length away from the fault, the 100-year return period pga for the azimuth-dependent model was 20% less than that estimated by the classical model.

The incorporation of azimuthal terms in ground motion prediction will have an important impact on seismic hazard mapping, because, as indicated, the shape of hazard contours around a fault will change significantly when faults are capable of focusing wave energy. When designing structures for seismic loads, the potential for azimuthal variations in ground motion response must be accounted for; it is preferable that this be accomplished by utilizing both theoretical information and empirical information as opposed to assuming that such effects are included in the uncertainty in the ground motion estimates.

Finally, the methods used here in the characterization of peak ground accelerations are directly applicable to the characterization of other ground motion response parameters, including peak ground displacements and velocities, rms amplitudes, durations, spectral amplitudes, and response spectra amplitudes. In fact, any characterizations routinely developed based on strong motion accelerograms can be implemented using the theoretical simulation model utilized in this work.

## REFERENCES

- Abrahamson, N. A., and R. B. Darragh (1985). "The Morgan Hill Earthquake of April 24, 1984 - The 1.29g Acceleration at Coyote Lake Dam: Due to Directivity, a Double Event, or Both?", Earthquake Spectra, Vol. 1, No. 3.
- Aki, K. (1979). "Characterization of Barriers on an Earthquake Fault," J. Geophy. Res., 84, 6140-6148.
- Anagnos, T. (1984). "A Stochastic Earthquake Recurrence Model with Temporal and Spatial Dependence," Ph.D. Dissertation, Dept. of Civil Engineering, Stanford University.
- Apsel, R. J. and J. E. Luco (1983). "On the Green's Functions for a Layered Halfspace, Part I," Bull. Seis. Soc. Am., Vol. 73.
- Apsel, R. J. and J. E. Luco (1983). "On the Green's Functions for a Layered Halfspace, Part II," Bull. Seis. Soc. Am., Vol. 73.
- Bakun, W. H., et al. (1984). "The 1984 Morgan Hill, California, Earthquake," U.S.G.S. Open File Report 84-498A, (Preliminary).
- Benjamin, J. R. and C. A. Cornell (1970). Probability, Statistics and Decisions for Civil Engineers, McGraw Hill Book Co., New York.
- Berardi, R., et al. (May 1981). "Campania-Lucania Earthquake on 23 November 1980 Accelerometric Recordings of the Main Quake and Relating Processing," Contributo Alla Caratterizzazione della Sismicita' del Territorio Italiano.
- Boatwright, J. and D. M. Boore (1982). "Analysis of the Ground Accelerations Radiated by the 1980 Livermore Valley Earthquakes for Directivity and Dynamic Source Characteristics," Bull. Seis. Soc. Am., Vol. 72, 1843-1865.

- Bolt, B. A. (1983). "The Contribution of Directivity Focusing to Earthquake Intensities," U.S. Army Corps of Engineers Miscellaneous Paper S-73-1.
- Bolt, B. A., et al. (1985). "The Morgan Hill Earthquake of April 24, 1984-- Seismological Aspects," Earthquake Spectra, Vol. 1, No. 3.
- Boore, D. M. and W. Joyner (1978). "The Influence of Rupture Incoherence on Seismic Directivity," Bull. Seis. Soc. Am., 68, 283-300.
- Boore, D. M. and W. Joyner (1982). "The Empirical Prediction of Ground Motion," Bull. Seis. Soc. Am., Vol. 72.
- Brady, A. G. and A. F. Shakal (1985). "The Morgan Hill Earthquake of April 24, 1985--Strong-Motion Records," Earthquake Spectra, Vol. 1, No. 3.
- Campbell, K. W. (1977). "The Use of Seismotectonics in the Bayesian Estimation of Seismic Risk," School of Engineering and Applied Science, University of California, Los Angeles, UCLA-ENG-7744.
- Campbell, K. W. (1981). "Near-Source Attenuation of Peak Horizontal Acceleration," Bull. Seis. Soc. Am., Vol. 71, 2039-2070.
- Chiaruttini, C. and L. Siro (1981). "The Correlation of Peak Ground Horizontal Acceleration with Magnitude, Distance, and Seismic Intensity for Friuli and Ancona, Italy, and the Alpid Belt," Bull. Seis. Soc. Am., Vol. 71.
- Cornell, C. A. (1968). "Engineering Seismic Analysis," Bull. Seis. Soc. Am., Vol. 58, 1583-1606.
- Das, S. and K. aki (1977). "Fault Planes with Barriers: A Versatile Earthquake Model," J. Geophy. Res., 82, 5648-5670.
- DerKiureghian, A. and A. H-S. Ang (1975). "A Line Source Model for Seismic Risk Analysis," Structural Research Series No. 419, University of Illinois at Urbana-Champaign.

- Esteva, L. (1969). "Seismicity Prediction: A Bayesian Approach," Proceedings of the Fourth World Conf. on Earthquake Engineering, 172-184.
- Fukao, Y. and K. Abe (1971). "Multimode Love Waves Excited by Shallow and Deep Earthquakes," *Bull. Earthquake Res. Inst., Tokyo University*, 49, 1-12.
- Gilbert, F. and A. M. Dziewonski (1975). "An Application of Normal Mode Theory to the Retrieval of Structural Parameters and Source Mechanisms from Seismic Spectra," *J. R. Astron. Soc.*, 278, 187-269.
- Hamilton, R. M. (1970). "Time-term Analysis of Explosion Data from the Vicinity of the Borrego Mountain, California Earthquake of 9 April 1968," *Bull. Seis. Soc. Am.*, Vol. 60, 367-381.
- Heaton, T. H. and D. V. HelMBERGER (1977). "A Study of the Ground Motion of the Borrego Mountain, California Earthquake," *Bull. Seis. Soc. Am.*, Vol. 67, 315-330.
- Heaton, T. H. and D. V. HelMBERGER (1978). "Predictability of Strong Ground Motion in the Imperial Valley: Modeling the M4.9 November 4, 1976 Brawley Earthquake," *Bull. Seis. Soc. Am.*, Vol. 68, 31-48.
- Herrmann, R. B. and M. J. Goertz (1981). "A Numerical Study of Peak Ground Motion Scaling," *Bull. Seis. Soc. Am.*, Vol. 71.
- Herrmann, R. B. and O. W. Nuttli (1975). "Ground Motion Modeling at Regional Distances for Earthquakes in the Continental Interior, I: Theory and Observations," Earthquake Engineering and Structural Dynamics, Vol. 4.
- Herrmann, R. B. and O. W. Nuttli (1975). "Ground Motion Modeling at Regional Distances for Earthquakes in the Continental Interior, II: Effect of Focal Depth, Azimuth, and Attenuation," Earthquake Engineering and Soil Dynamics, Vol. 4.

- Idriss, I. M. (1978). "Characteristics of Earthquake Ground Motions," Proceedings of the ASCE Specialty Conference on Earthquake Engineering and Soil Dynamics, Vol. III, Pasadena, California.
- Joyner, W. B., and D. M. Boore (1981). "Peak Horizontal Acceleration and Velocity from Strong Motion Records Including Records from the 1979 Imperial Valley, California Earthquake," Bull. Seis. Soc. Am., Vol. 71.
- Kanamori, H. (1970). "Synthesis of Long-Period Surface Waves and Its Application to Earthquake Source Studies -- Kurile Islands Earthquake of October 13, 1963," J. Geophys. Res., 75, 5011-5027.
- Kanamori, H. and Cipar (1974). "Focal Processes of the Great Chilean Earthquake May 22, 1960," Physics of the Earth and Planetary Interiors, Vol. 9.
- Kanamori, H. and G. Stewart (1976). "Mode of Strain Release Along the Gibbs Fracture Zone, Mid-Atlantic Ridge," Physics of the Earth and Planetary Interiors, Vol. II.
- Kiremidjian, A. S. (1976). "Probabilistic Hazard Mapping and Development of Site-Dependent Seismic Load Parameters," Ph.D. Dissertation, Dept. of Civil Engineering, Stanford University.
- McCann, M. W. (1981). "A Bayesian Geophysical Model for Seismic Hazard," Blume Center Technical Report No. 47, Stanford University.
- McGuire, R. K. (1974). "Seismic Structural Response Risk Analysis, Incorporating Peak Response Regressions on Earthquake Magnitude and Distance," Report R74-51, Dept. of Civil Engineering, MIT.
- Mortgat, C. P. (1976). "A Bayesian Approach to Seismic Hazard Mapping: Development of Stable Design Parameters," Ph.D. Dissertation, Dept. of Civil Engineering, Stanford University.

- Raiffa, H. and R. Schlaifer (1961). Statistical Decision Theory, MIT Press, Cambridge.
- Savy, J. B. (1982). "Use of an Artificial Catalog of Earthquake Data in a Study of the Attenuation and Component Statistics of the Strong Ground Motion Acceleration," Research Rep. 82-02, 121 pp., Dept. of Materials Science and Engineering, MIT, Cambridge.
- Schoof, C. C. (1984). "Geophysical Input for Seismic Hazard Analysis," Ph.D. Dissertation, Department of Civil Engineering, Stanford University.
- Shah, H. C., C. P. Mortgat, A. S. Kiremidjian, and T. C. Zsutty (1975). "A Study of Seismic Risk for Nicaragua, Part I," The John A. Blume Earthquake Engineering Center Technical Report No. 11, Dept. of Civil Engineering, Stanford University, California.
- Singh, J. P. (1985), Earthquake Ground Motions: "Implications for Designing Structures and Reconciling Structural Damage," Earthquake Spectra, Vol. 1, No. 2.
- Singh, J. P. (1982). "Seismic Source Directivity Evidence from the August 6, 1979 Coyote Lake Earthquake," Proceedings, Conf. on Earthquake Hazards of the Eastern San Francisco Bay Area, Hayward, California, California Division of Mines and Geology.
- Swanger, H. W. and D. M. Boore (1978). "Simulation of Strong Motion Displacements Using Surface Wave Modal Superposition," Bull. Seis. Soc. Am., Vol. 68, 907-922.
- Toro, G. R. (1981). "Biases in Seismic Ground Motion Prediction," Research Rep. R81-22, 133 pp., Dept. of Civil Engineering, MIT, Cambridge.
- USGS Open-File Report 79-1654 (1979). "Preliminary Summary of the U.S. Geological Survey Strong-Motion Records from the October 15, 1979 Imperial Valley Earthquake."

Wang, C. Y. and R. B. Herrmann (1980). "A Numerical Study of P, SV, and SH Wave Generation in a Plan Layered Medium," Bull. Seis. Soc. Am., Vol. 70.

APPENDIX A -  
 MODELING OF THE STRONG GROUND MOTION RESPONSE AT  
 STATION ELC DURING THE 1968 BORREGO MOUNTAIN EARTHQUAKE

The synthetic acceleration and displacement response at Station ELC computed for the 1968 Borrego Mountain earthquake are compared with the observed records for this event. The earth structure used is given in Table 3 in Section 2.2, and the fault rupture characteristics are as shown below in Table A-1.

**Table A-1**  
**Source Parameters for the 1968**  
**Borrego Mountain Earthquake**

$M_0$	$6.9 \times 10^{25}$ DYNE-CM
Mean Depth	6.5 km (4-9 km)
Rise Time	0.75 sec (boxcar)
Rupture Velocity	2.7 km/sec (5 km toward ELC; 4 km away from ELC)
Q	200
$\delta$	90°
$\lambda$	0°

Figure A.1 shows the observed acceleration waveform (N-S component) at ELC (top curve), and the simulated time history (2nd curve). The remaining curves represent the acceleration response for each overtone which are summed to obtain the simulated response. Excellent agreement is noted between the observed and simulated time histories, both in terms of amplitude and frequency content<sup>†</sup>, as well as with respect to phase arrivals. High frequency body waves (higher overtones) dominate the response in the early part of the

<sup>†</sup> The observed time history has been low-pass filtered at 5 Hz.

record ( $t = 15$  to  $30$  sec.) while long period surface waves (lower overtones) dominate during the latter part of the record.

The displacement responses for this event are shown in Figure A.2. The synthetic displacements were simulated using the same earth structure and source parameters used in modeling the acceleration response. Again, excellent agreement is achieved throughout the record.

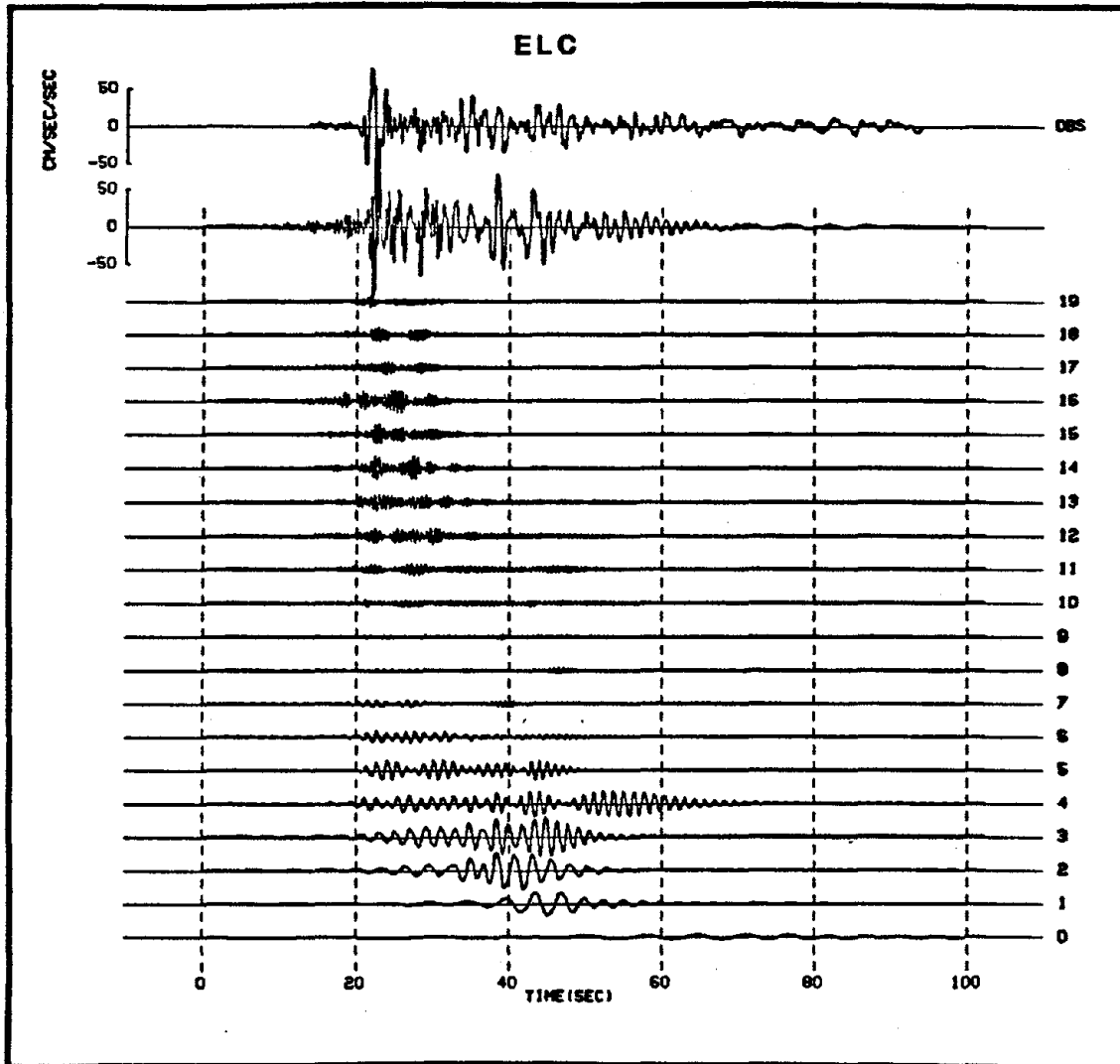


Figure A.1. Comparison of the observed and theoretical acceleration response at station ELC during the 1968 Borrego Mountain earthquake. In this example, the fundamental mode and first 19 overtones are summed to compute the total SH and P-wave response, which yields excellent agreement with the observed acceleration response.

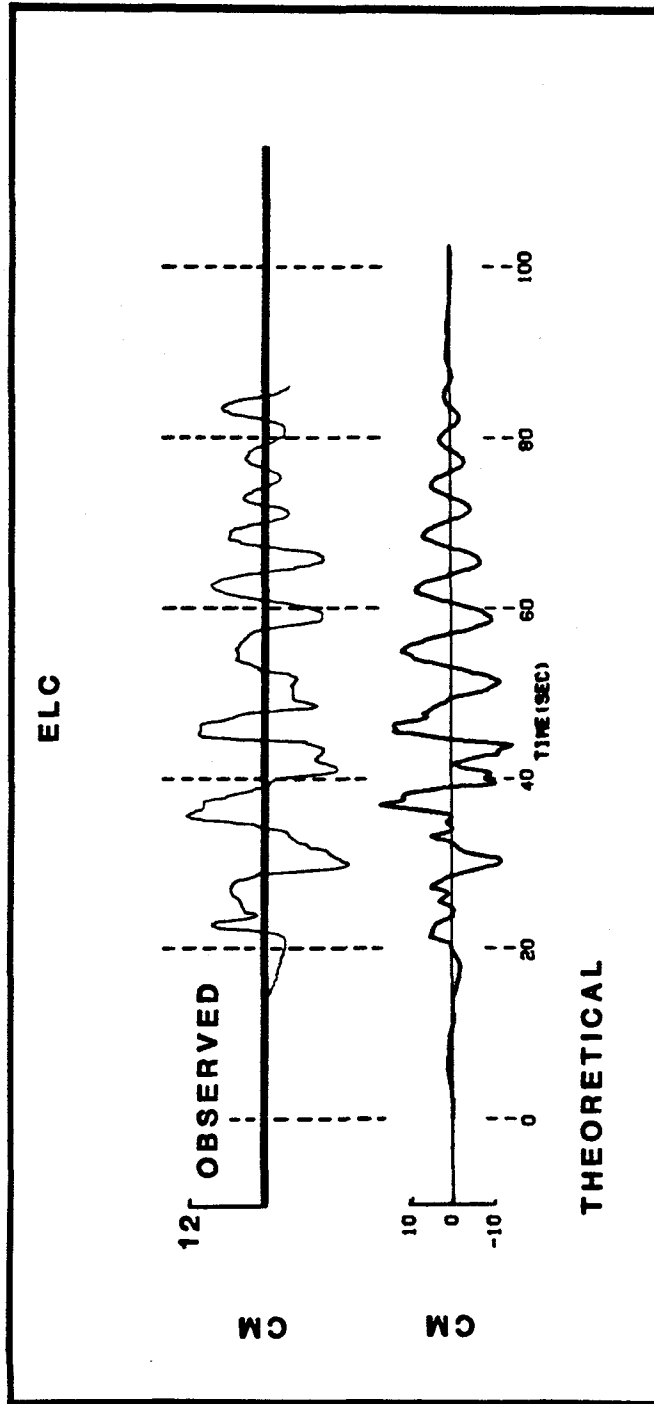


Figure A.2. Observed and theoretical displacement response at station ELC during the 1968 Borrego Mountain earthquake.

## APPENDIX B - SIMULATED ACCELERATION TIME HISTORIES

The time histories for four simulations corresponding to HHR0, HHR1, HHR2, and HHR5 are shown for sites of epicentral distances ranging from 10 km to 80 km, and epicentral azimuths ranging from 0 to  $\pi$ . Each fault is assumed to have the major extent of rupture to the north ( $\phi = 0$ ). The component with the maximum acceleration is shown in each figure. The epicentral distance and azimuth, dislocation, rise time, and rupture velocity for each simulation is also given.

The figures are set up in a matrix recorded on microfiche where each row corresponds to a single distance, and each column corresponds to a different azimuth as shown below:

decreasing distance/increasing azimuth  $\longrightarrow$   
 $\downarrow$

Rows 1-15 correspond to HHR0, 16-30 correspond to HHR1, 31-45 correspond to HHR2, and 46-60 correspond to HHR5.

**APPENDIX B**

**SIMULATED ACCELERATION TIME HISTORIES**

## APPENDIX C - RECIPIENTS OF PHASE I RESEARCH RESULTS

1. Professor Haresh C. Shah, Department of Civil Engineering, Stanford University.

